Journal of Structural Geology 85 (2016) 95–114

Contents lists available at ScienceDirect

Journal of Structural Geology

journal homepage: www.elsevier.com/locate/jsg

Structural and statistical characterization of joints and multi-scale faults in an alternating sandstone and shale turbidite sequence at the Santa Susana Field Laboratory: Implications for their effects on groundwater flow and contaminant transport

Antonino Cilona [a, *], Atilla Aydin [a], Jeremias Likerman [b], Beth Parker [c], John Cherry [c]

[a] Department of Geological and Environmental Sciences, Stanford University, Stanford, CA, 94305, USA
[b] Laboratorio de Modelado Geológico (LaMoGe), Instituto de Estudios Andinos Don Pablo Groeber, Universidad de Buenos Aires, Ciudad Universitaria, C1428EHA, Buenos Aires, Argentina
[c] G360, Centre for Applied Groundwater Research, School of Engineering, University of Guelph, Guelph, Ontario, N1G 2W1, Canada

ARTICLE INFO

Article history:
Received 3 March 2015
Received in revised form
1 February 2016
Accepted 10 February 2016
Available online 11 February 2016

Keywords:
Joint zones
Fracture attributes
Fault zone hierarchy
Fracture dimensional parameters
Fluid flow

ABSTRACT

This paper describes the properties of faults and fractures in the Upper Cretaceous Chatsworth Formation exposed at Santa Susana Field Laboratory and its surroundings (Simi Hills, California), where groundwater flow and contamination have been studied for over three decades.

The complex depositional architecture of this turbidite consisting of alternating sandstones and shales, interacting with formative stress conditions are responsible for multi-scale fault hierarchies and permeable fractures in which nearly all groundwater flow occurs.

Intensity and distribution of background fractures and their relation to bedding thickness are established for sandstones, the dominant lithology. The architecture of faults with increasing displacement is described, and relationships among fault dimensional parameters captured.

Data from ~400 boreholes and piezometers reveal the effect of faults and fractures on groundwater flow. Large hydraulic head differences, observed across fault zones with shale-rich cores, indicate these structures as cross-flow barriers. Moreover, hydraulic head profiles under ambient conditions, and pumping tests suggest strong hydraulic connectivity in all directions to depth of hundreds of meters.

This outcrop-based structural characterization relates the horizontal hydraulic conductivity to the observed well-connected fracture network, and explains the strong vertical connectivity across low-hydraulic conductivity shales as faults and sheared fractures provide flow pathways.

1. Introduction

The Santa Susana Field Laboratory (SSFL) in Simi, California, has been subjected to intensive investigations of groundwater contamination in the sedimentary bedrock since the 1980s. The bedrock belongs to the Upper Cretaceous Chatsworth Formation, which is a turbidite composite sequence comprised of sandstones as the dominant lithology with lesser siltstones and conglomerates interbedded with shales (Colburn et al., 1981; Link et al., 1984).

Numerous boreholes continuously cored and an extensive groundwater monitoring network (~400 boreholes and piezometers) to maximum depths of 300 m below ground surface, record the hydrogeologic conditions governing the migration of contaminants, with trichloroethylene (TCE) of primary interest (Sterling et al., 2005; Cherry et al., 2009). Previous hydrogeological studies indicate that fractures govern the hydraulic conductivity, commonly with one-to-three permeable fractures per vertical meter in the sandstone (Quinn et al., 2015, 2015b). These smaller fractures along with larger faults have determined the nature of the contaminant plumes that have developed over the past few decades (Cherry et al., 2009). Yet, despite general recognition of the influence of fractures and faults on groundwater flow and contaminant transport, so far there has been no systematic structural analysis of the fault and fracture system at the Santa Susana Field Laboratory. Thus, an outcrop-based structural characterization of the area was needed to understand features observed in

* Corresponding author.
E-mail address: cilona@stanford.edu (A. Cilona).

http://dx.doi.org/10.1016/j.jsg.2016.02.003

boreholes, for obtaining better projections of features of hydrogeological importance between boreholes and from groundwater recharge areas on-site to groundwater discharge areas on and off-site.

The present contribution aims to bridge this gap by first describing the mechanisms responsible for nucleation and development of fault zones at SSFL, and then establishing hierarchical classes among the faults. Additionally, the study defines relationships among the main fault dimensional parameters (length, width, and displacement) and provides quantitative data on background (non-fault-related) fractures and their terminations. With this information and analysis, we developed a conceptual model of the nucleation and development of the fault and fracture system at SSFL to explain the contrast in hydraulic behavior of fault zones, which are barriers to cross-flow in some sectors of the study area and not others. Overall, this paper provides structural insights that enable interpreting previous hydrogeological observations, including hydraulic head profiles indicating position of hydraulic unit boundaries as presented by Meyer et al. (2014).

2. Geological setting

The Santa Susana Field Laboratory is located in the Simi Hills, about 65 km northwest of downtown Los Angeles in southern California. The area is bounded to the north by the Simi Valley, to the west by the San Fernando Valley, and to the south by the Santa Monica Mountains (Fig. 1a). The Simi Hills occupy a portion of the easternmost Western Transverse Ranges province, which is known for its relatively young intense deformation (Yeats et al., 1994; Langenheim et al. 2011). This province, extends east-west across the San Andreas Fault zone, and experiences north-south shortening (Fig. 1a). In the area, faults and folds are mainly oriented east-west (Langenheim et al. 2011). The northern margin of the Simi Hills is marked by a steep topographic front defined by the Simi Valley and the Santa Susana thrusts. These faults are parts of a discontinuous, predominantly north-dipping thrust belt extending from the Santa Barbara Channel (SBC) on the west to about 200 km to the east (Fig. 1a). The Paleogene and Cretaceous rocks cropping out in the Simi Hills trend northeast-southwest and are bounded by the Chatsworth Reservoir and North Reservoir faults (Fig. 1b).

The Western Transverse Ranges block rotated about 90° around a vertical axis located near its present southeast corner (Nicholson et al., 1994; Langenheim et al., 2011). This clockwise rotation began in early-Middle Miocene time and is considered a major element of the Neogene tectonic evolution of southern California.

SSFL and its immediate surroundings include rocks ranging from late Cretaceous to late Pliocene. One of the oldest units in this area is the Upper Cretaceous Chatsworth Formation (Fig. 1b). This formation is conformably overlaid by a 3 km-thick sequence of sedimentary rocks, which ages range between Upper Cretaceous and early Miocene. In the early Miocene, the area experienced uplift, tilting, and significant erosion. The presence of late Miocene rocks unconformably lying on the late Cretaceous and early Tertiary formations suggests that by mid-to-late Miocene the erosion

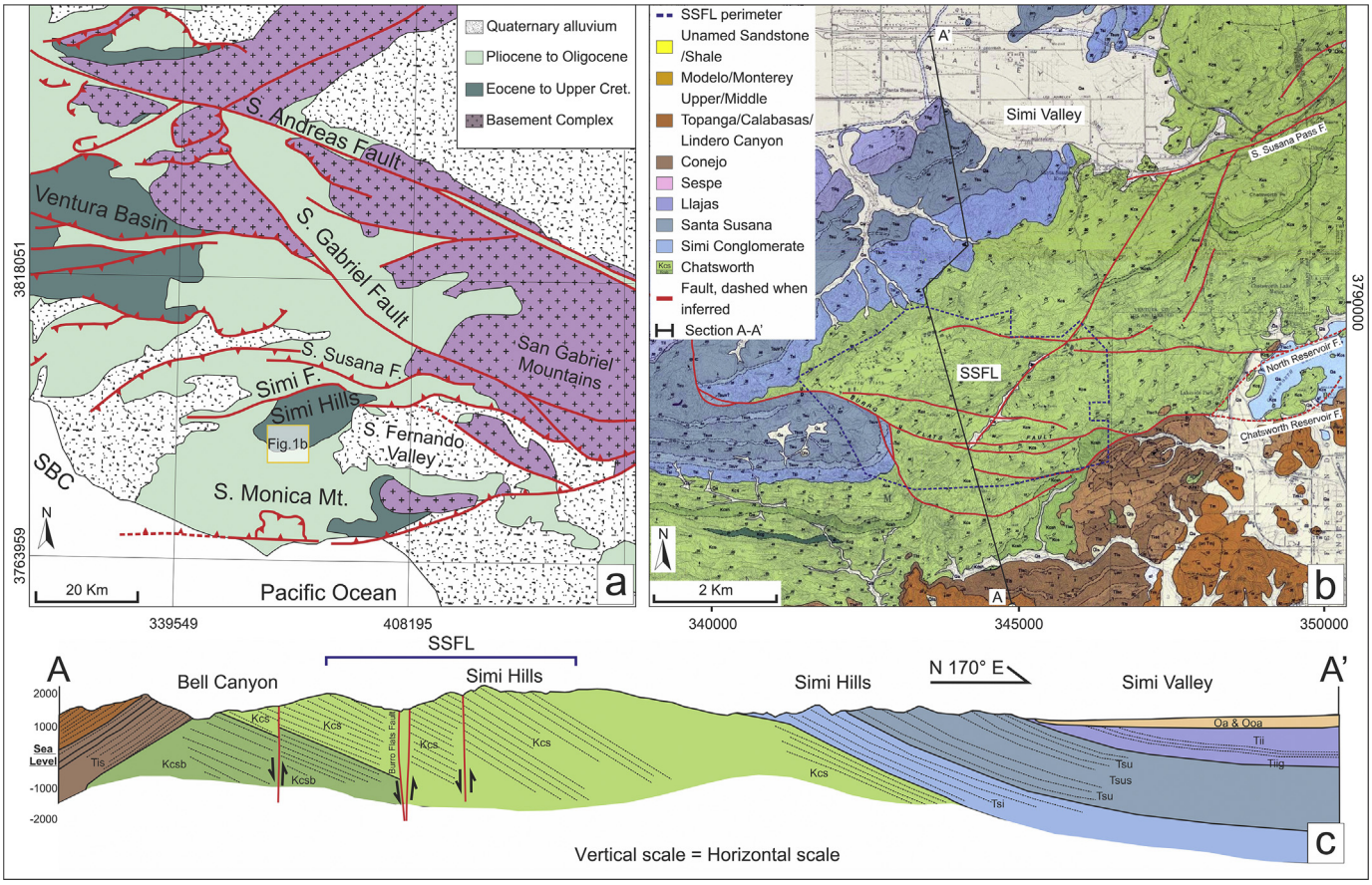

Fig. 1. a) Structural map of the Western Transverse Ranges and its surroundings (modified from Jennings and Strand, 1969). Faults are represented in red. Number represent the UTM 11S coordinates. The yellow rectangle bounds the extents the map shown in b; b) Geological map (number represent the UTM 11S coordinates) and cross section (c) of SSFL (blue polygon) and its surroundings, modified from Dibblee (1992).

exposed the early Tertiary and late Cretaceous formations, (Fig. 1b; Yerkes and Campbell, 2005; MWH, 2007).

Fig. 1c displays a N–S oriented geological section cutting across SSFL. In this cross section (modified from Dibblee, 1992), the Chatsworth Formation is interpreted to be the limb of a relatively older anticline or monocline. The bedding typically strikes approximately N70°E and dips 25°–35° to the northwest.

2.1. The Chatsworth Formation

The Chatsworth Formation is a composite turbidite sequence that was deposited in a mid-fan environment (Link et al., 1984). This formation, which extensively crops out in the study area, consists primarily of sandstone with interbedded shale, siltstone, and conglomerate (Fig. 2a). In the vicinity of SSFL, the Chatsworth Formation is informally subdivided in two parts: upper and lower (Montgomery and Watson, 2000). The lower Chatsworth Formation contains a greater proportion of fine-grained deposits than the upper one. The stratigraphy of the upper part consists of alternating coarser- and finer-grained lithofacies (Fig. 2a). The coarser lithofacies are primarily made up of medium-to fine-grained sandstones. Intervals of stacked sandstone beds with few or no fine-grained interbeds or bedding partings reach a few meters thickness and may extend laterally for hundreds of meters.

The fine-grained lithofacies (heteroliths) typically contain 50 percent or more shale interbedded with lesser amounts of siltstone and sandstone. Individual beds are less than one meter thick and usually less than 30 cm thick (MWH, 2009).

The upper Chatsworth Formation comprises two sandstone-dominated sequences, referred within the study area as Sandstone 1 and 2, respectively (Fig. 2a; MWH, 2009). These two turbiditic sequences represent two periods of activity of the fan. Both sequences are bounded above and below by fine-grained lithofacies referred to from bottom to top as Shale 1, 2, and 3, respectively (MWH, 2009). These shales mark time intervals of inactivity of the turbiditic fan and are often associated to a rise of the sea level (Di Celma et al., 2011). Both Sandstone 1 and 2 are further subdivided into three fining-upward cycles (Fig. 2a).

The sandstones and siltstones of the Chatsworth Formation have an arkosic composition (Twenter and Metzger, 1963) with an average compositions of quartz 33 ± 9%, plagioclase 33 ± 7%, and K-feldspar 20 ± 6%. Additionally, ~5% is represented by lithic fragments, and 9.7 ± 6% phyllosilicate minerals. Among these phyllosilicates biotite, and chlorite are the most common, but also muscovite and clay (illite, vermiculite, smectite and kaolinite) are present (Loomer et al., 2009). The average porosity values range from 1% to 11.5%. The fine-grained lithofacies are composed of: quartz (mean value: 22.48%), plagioclase (mean value: 21.08%), K-feldspar (mean value: 23.56%), mixed-layered minerals - illite-smectite (mean value: 15.26%), clinochlore (mean value: 12.4%), illite (mean value: 5.21%). Calcite is the dominant cement in the Chatsworth Formation, however several sedimentary layers have quartz cement (MWH, 2009). Hurley (2003) derived the uniaxial compressive strength (UCS) of sandstones and shales from the Chatsworth Formation by means of Smith hammer measurements. This author assessed over ~700 m of cores recovered from three boreholes within SSFL perimeter. His results show that the sandstones have an average UCS of 40 MPa (ranging between 23 and 140 MPa) and the shales have an average UCS of 25 MPa (ranging between 21 and 30 MPa), significantly lower than that for the sandstone units.

2.2. Deformation of turbidite sequences

Aquifers may have both vertical and lateral porosity, permeability and capillarity heterogeneities (Bense et al., 2013). In

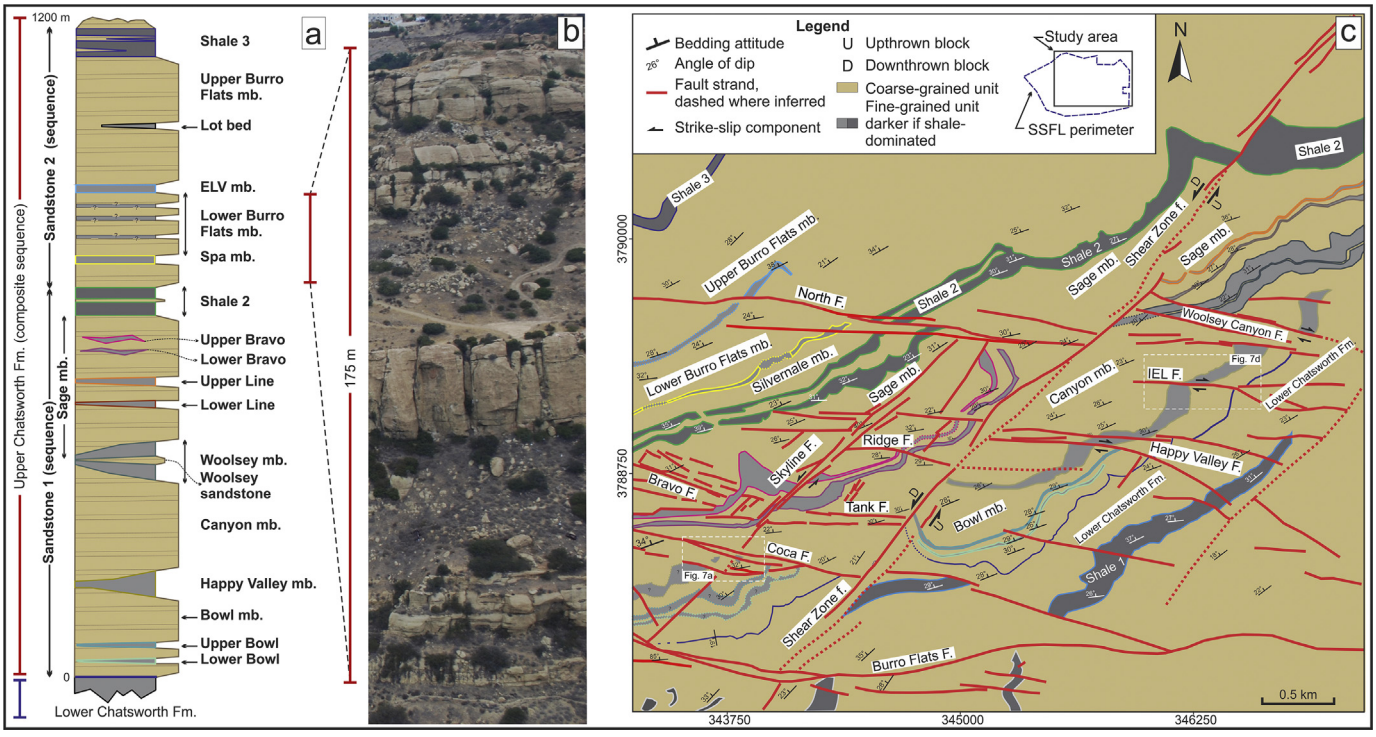

Fig. 2. a) Stratigraphic column of the upper Chatsworth Formation in the vicinity of the study area. The thicknesses of the major units are to scale except that the thicknesses of the thin interbeds are exaggerated. Modified from MWH (2009). b) Helicopter image of the portion of Chatsworth Fm. between Lower Burro Flats and Silvernale members showing alternating sandstones and shale at different scales. c) Simplified geological map of the study area showing ESE–WNW and NE–SW trending fault sets cutting across the Chatsworth Formation (modified from MWH, 2009). Sandstone units are represented in khaki; shale and fine-grained units in different tints of grey.

siciliciclastic rocks, these heterogeneities occur at various scales, and may be responsible for significant variations in the rock petrophysical parameters. The heterogeneities can result from depositional facies and diagenesis, as well as faults and fractures (De Ros, 1998; Schulz-Rojahn et al., 1998; Aydin, 2000). Siliciclastic turbidites are the products of deepwater channels and avalanches, and they primarily consist of sandstones and shales of various thicknesses. Sandstones and shales may interlayer and interfinger forming complex sedimentary architectures, which controls sand body geometry and mud/sand ratio (Di Celma et al., 2011). These architectures influence geometry and distribution of subsequent fractures as well as the rate and pathways of groundwater flow (Wardlaw and Taylor, 1976; Weber, 1982; Florez-Niño et al., 2005; Bense and Person, 2006; Gonzales and Aydin, 2008). Due to their different rheology, sandy and muddy lithologies respond to stress differently, resulting in fracture populations with distinct types, geometries and spatial distributions as a function of sedimentary body geometries and distributions (Gross et al., 1995; Bertotti et al., 2007; Laubach et al., 2009).

The three most common lithologies at SSFL are stiff sandstones, soft shales/siltstones, and stiff shales/siltstones. Low-porosity stiff sandstones tend to deform brittlely producing opening-mode fractures such as joints and joint zones (Hodgson, 1961; Laubach, 1992; Cruikshank and Aydin, 1995). When stress acts upon flat-lying beds, these fractures are generally oriented roughly perpendicular to bedding and localize within competent layers (Hodgson, 1961; Bai et al., 2000). Individual fractured units, defined by the stratigraphic localization of bed-perpendicular fractures, generally correspond to the stratigraphically controlled differences in the mechanical properties of beds and interfaces (Laubach et al., 2009; Gudmundsson et al., 2010). Joints propagate in-plane across the layered rocks terminating against the fractured units boundaries, which often are thin shale layers or bedding partings (Pollard and Aydin, 1988; Helgeson and Aydin, 1991; Shackleton et al., 2005; Cooke et al., 2006; Gudmundsson, 2011; Rustichelli et al., 2013).

Both joints and joint zones provide weak locations for later shearing, leading to nucleation and propagation of faults (Myers and Aydin, 2004; Flodin, and Aydin, 2004; de Joussineau and Aydin, 2007; Aydin and de Joussineau, 2014). This faulting mechanism is influenced by geometry and distribution of the pre-existing joints, and may produce faults with great extents through linkage of neighboring fractures and fault segments. The progressive geometric evolution of a linkage zone is one of the key parameters to evaluate for both lateral and vertical continuity of a fault zone (Martel et al., 1988; Cartwright et al., 1995; Peacock and Parfitt, 2002; Davatzes and Aydin, 2003; Kim et al., 2004; de Joussineau and Aydin, 2007).

The response to stress of shales can be substantially different from those of the adjacent sandstones (see Gale et al., 2014 for a full review). Soft shales accommodate strain by diffuse ductile deformation (Chong and Smith, 1984) and prevent joint propagation (Helgeson and Aydin, 1991; Aydin, 2014). Whereas, shales that had undergone mechanical compaction and lithification are stiff and deform brittlely (Engelder et al., 2009; Aydin, 2014). Shales play a fundamental role also in the characterization of fault-sealing potential (Yielding et al., 1997). Indeed, soft shales tend to smear along the faults (Aydin and Eyal, 2002; Cilona et al., 2015) reducing the permeability and increasing the capillary, of the fault rock in a direction perpendicular to the smear zone (Eichhubl et al., 2005).

Given factors such as joint development as a function of lithology and layer geometry, fracture reactivation during a history of changing stresses and the influence of rock properties on fault-zone permeability, predicting the fluid pathways within fractured turbidite bodies of sandstones and shales with various rheological properties is challenging (Aydin, 2000; Faulkner et al., 2010).

3. Methods

This paper combines field-based structural analysis with image analysis of multi-scale structural maps to characterize the architecture, geometry, and spatial distribution of the structures within the Chatsworth Formation at SSFL. Available stratigraphic and structural data (main source MWH, 2009) were verified to assess the distribution of lithologies (coarse- and fine-grained dominated) and structures (joints, joint zones, deformation bands and fault zones) within different portions of the Chatsworth Formation. Where relevant to the structural characterization, stratigraphic data such as thickness and lateral extents of single beds or mechanical units containing multiple beds were collected.

The field campaigns aimed at establishing the joint patterns, and the type and hierarchy of faults based on dimensional parameters (length, width, and displacement). This task was carried out at key outcrops where the structures are better exposed. Following a qualitative evaluation of each structural station, we collected quantitative structural data for both background and fault-related fractures. Tens of outcrops were studied by combining detailed (1:1 to 1:10 scale) structural maps and scanline surveys. For this study, we collected data both from map (generally pavements corresponding to dip slope surfaces) and section view. This approach allowed us to constrain the 3D geometry of joints and faults, as well as reducing the sampling bias caused by the orientation of individual outcrops.

The distribution of non-fault-related fractures, mostly joints, was established through bed-parallel scanlines performed along sandstone beds located far from any major fault zone. Seven different sandstone beds ($0.05 < \text{thickness} < 5$ m), bounded on top and bottom by fine-grained beds were studied to assess the role of bed thickness on joint spacing (Bai and Pollard, 2000). These sandstone beds were selected because of the exceptional quality of the outcrops and fracture patterns differ from adjacent beds. The scanlines were performed in the middle of the single beds, and had lengths of around ten times the bed thickness, which according to Ortega et al. (2006) is a representative length. We measured the attitude of each discontinuity intersected along the scanline and its distance from the scanline origin. For each fracture set, the spacing was computed separately. Then a trigonometric correction based upon the fracture orientation with respect to the scanline orientation was applied to convert the apparent spacing into real spacing (Terzaghi, 1965). Several indices were calculated from scanline data: fracture spacing index (FSI), fracture spacing ratio (FSR), fracture saturation (S/T) and coefficient of variation (Cv), and are defined below.

(i) FSI is the slope of the regression line of mechanical unit thickness versus median joint spacing (Narr and Suppe, 1991).
(ii) FSR is the thickness of a mechanical unit divided by the median joint spacing within that mechanical unit (Gross, 1993).
(iii) S/T is the ratio between the mean joint spacing and the corresponding mechanical unit thickness (Wu and Pollard, 1995).
(iv) Cv is the ratio between the standard deviation of a joint spacing dataset and its mean value (Gillespie et al., 1993).

FSI and FSR describe the fracture intensity. S/T is employed when focusing on joint spacing and joint saturation within a given medium. Cv indicates whether a joint distribution is clustered or not. If Cv is close to 0, joints are evenly spaced, close to 1 indicates that joints are randomly distributed, and greater than 1 means that they are clustered.

A second set of measurements was collected across and along individual fault zones. We produced detailed structural maps from ground and aerial (low-altitude drone, helicopter and satellite) images and used them to characterize the fault zone architectures. From scanline surveys, we assessed the values for apparent spacing of the main sets of structures (joints, joint zones, and faults). Because the structures have very steep dip angles (dip>70°), the apparent spacing represents a good approximation to the real spacing.

The same maps were also used to calculate the lengths of the sampled structures. The lengths were obtained by using the image analysis software PCAS (Liu et al., 2013). The software was applied on rectified images, and provided length values in pixels, which were converted into meters using a simple proportionality constant. Cumulative frequency distribution graphs fitted by negative power-law were used to plot the populations of lengths (Mandelbrot, 1983):

$$N_{(\geq S)} = aS^{-D} \quad (1)$$

where N is the number of features longer than or equal to "S", "a" is a measurement of the sample size, and the power-law exponent D represents the slope of the best fit line, which has been interpreted as the fractal dimension by some authors (Childs et al., 1990; Scholz and Cowie, 1990). Populations of faults and fractures with characteristics that have distributions that yield a power-law exponent may be treated as scale-invariant, which means that the characteristics are consistent with changes in the scale of sampling for the population. This invariance allows the estimation of the aggregate properties of the rock across a range of length scales (cf. Twiss and Marrett, 2010).

Where good exposure and reliable stratigraphic markers were available, we collected data about the total fault zone width (fault core plus fault damage zone) and fault displacement. Length, width and maximum displacement values were plotted in logarithmic graphs to establish correlations between the two sets of parameters across a range of length scales (see Torabi and Berg, 2011).

4. Results

4.1. Fault network at SSFL

At the Santa Susana Field Laboratory, the Chatsworth Formation is crosscut by two dominant sets of faults: one trending NE–SW and generally showing apparent left-lateral strike-slip and another roughly oriented ESE-WNW showing apparent right-lateral strike-slip (Fig. 2c). However, both fault sets have evidence for a component of dip-slip motion. Many faults shown in Fig. 2c were briefly described in previous unpublished reports (MWH, 2007, 2009, Appendix 4-J).

4.2. Joints and joint clusters

Joints commonly show a negative relief and sometimes their surfaces display typical plumose structures with hackles, arrest lines and fringes, consistent with their formation as opening-mode fractures (Pollard and Aydin, 1988). Multiple sets of joints were identified in different portions of SSFL, however two sets of orthogonal joints, oriented roughly perpendicular to bedding, were observed in all studied outcrops of the Chatsworth Formation (Cilona et al., 2015). These two joint sets strike approximately NE–SW and NW–SE, parallel and perpendicular to the bedding strike, respectively (Fig. 3). The dip angles of both sets range between 65° and 90°. Both sets of joints show mutual abutting relationships, which implies that they formed contemporaneously. Although the age of these joints is not fully constrained, they likely formed prior to tilting because they are perpendicular to bedding.

At the Santa Susana Field Laboratory vein fillings are not common with only less than 5% of the sampled joints having an infilling. Systematic investigation of the infilling minerals were not performed in this study. However, based on handlens observations, calcite is the most common infilling mineral followed by quartz (MWH, 2009).

Following the classification for height distributions in Hooker et al. (2013), the joint populations at SSFL could be defined as hierarchical, where a range of fracture heights closely follows a range of interbedded fractured-layer thicknesses. However, even though within a fractured unit, most of the tallest fractures end at the same stratigraphic position, a wide range of smaller heights also occurs. The boundaries of single fractured units may be either fine-grained interbeds or open or sheared bedding partings.

The joint sets sometimes include arrays of closely spaced joints localized within narrow zones (Hodgson, 1961; Laubach, 1991, 1992). The geometry of such arrays may vary from completely overlapping sub-parallel joints to *en échelon* arrangements. In the literature, these structures are usually referred to as joint zones (JZs), joint clusters, fracture corridors, and joint swarms (Ogata et al., 2014). The term fracture corridor is more commonly used in the oil and gas industry.

Joint zones have a marked negative relief with respect to the surrounding host rock because they are more easily eroded (Fig. 4a). These zones represent preferential pathways for surface run-off, and are often vegetated and covered by debris. When observed at a scale of meters to 100s of meters, JZs are few meters wide and may reach lengths of several 10s of meters. These zones are composed of assemblages of discontinuous individual joints at SSFL (Figs. 4b and 5b).

The width of a joint zone is determined by the number and spacing of the joints that it encompasses; this number typically varies along single JZs. Considering one study site, the sampled JZs have width varying between two and four meters, whereas the number of joints within the single joint zone ranges from one at the tips to about eight in the central portions (Fig. 4b, c). These features can also be easily identified in borehole images (Fig. 5c). As expected, joint zones as clusters of joints have zone lengths that are greater than trace lengths of the individual joints they contain and may have greater heights as well, although they still generally terminate at shale-rich layers with thicknesses greater than ~10 cm (Fig. 5).

Both joints and joint clusters occasionally show evidence of reactivation in a primarily strike-slip sense (Fig. 3), however many examples of dip-slip shearing were documented. Splay joints (SPJ) are common in the extensional quadrants of sheared joints and joint zones, and tend to form clusters with lengths limited by the spacing of older fractures. SPJs often act as a link between neighboring joints, locally increasing their connectivity and effective lengths (Fig. 3). Moreover, splay joints have been used as kinematic indicators where they are co-planar to the local maximum compressive stress (de Joussineau et al., 2007).

4.3. Fault zones

Because fault architecture is strongly influenced by geometry and distribution of the preexisting joints and JZs at SSFL, the initial geometries of faults vary greatly. For example, faults form on one joint or link several joints, accommodating centimeter to decimeter-scale offsets (Figs. 3b, 5b and 6).

Sheared JZs produce relatively wide fault-zones. At the initial stage of evolution, fault zones have a discontinuous geometry, and because of their limited offsets, they do not cut across relatively thick fine-grained beds (Fig. 6a). With greater displacement, both

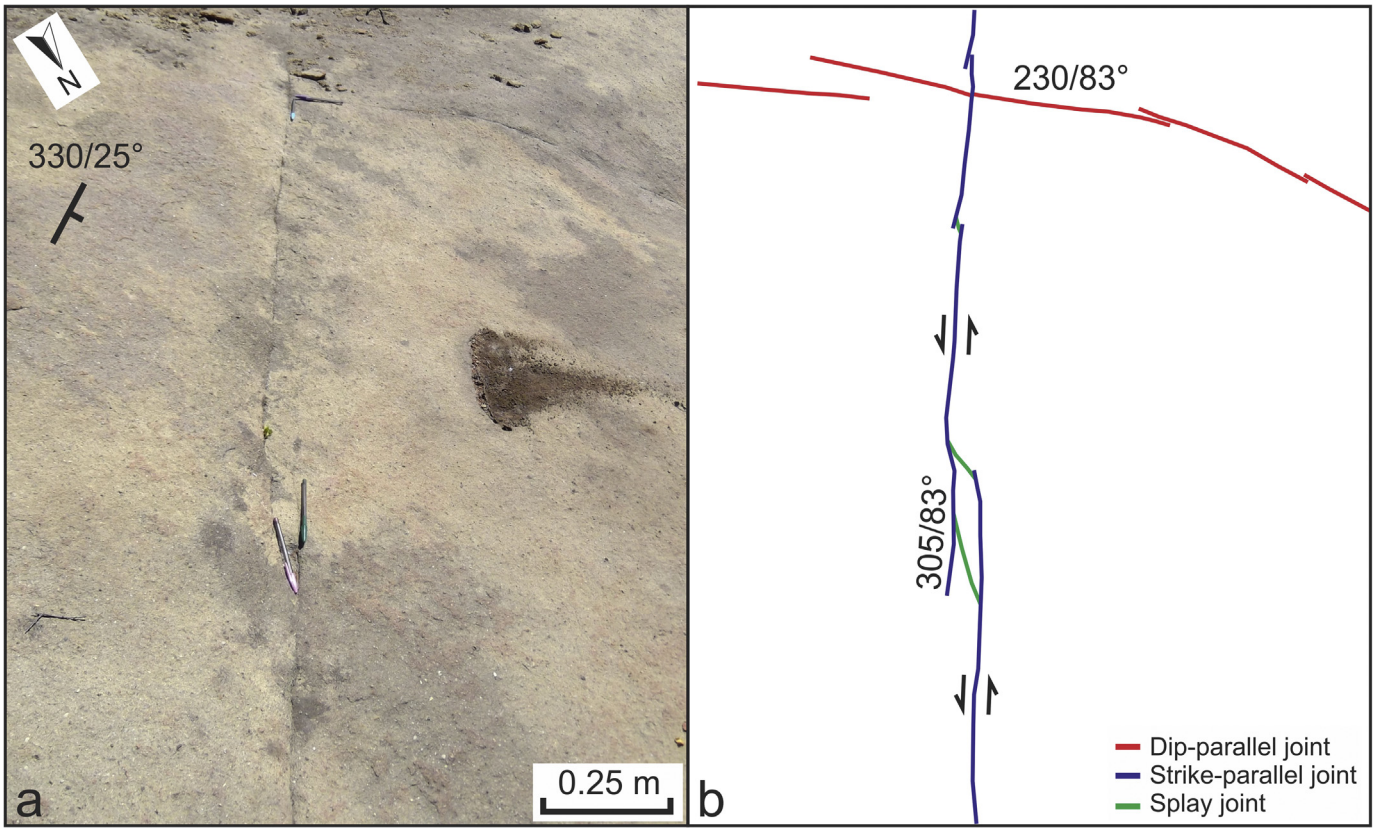

Fig. 3. a) Dip slope exposure; b) interpretation showing the dip-parallel (red) and strike-parallel (blue) joints. The strike-parallel set was reactivated as a left-lateral shear, which is consistent with the location of splay joints shown in green.

lateral and vertical extent of these structures increase by linking neighboring strands (Fig. 6b). With displacement increase, fault-core structure evolves, and pockets of fault rock develop (Fig. 6c).

Faults with meter-scale displacements (here referred to as small faults) have well-developed slip surfaces and few-to-ten centimeter wide pockets of fault rock (Fig. 6d). At linkages, the width of small faults is greater than elsewhere along the fault traces due to large number of splays therein. At this stage, lenses of slightly deformed sandstones are bound by the main slip surfaces. In general, the number of fractures in damage zones decreases outward from the center, but it is greater than the number of fractures in the surrounding host rocks (de Joussineau and Aydin, 2007).

Faults with a few meters-to-about ten meters displacement (here referred to as intermediate faults) display continuous slivers of fault rock along the main slip surfaces. The damage zones of such faults can reach several meters in width, and contained smaller secondary faults. Intermediate faults with sufficient displacements to offset thin shale packages (Fig. 6e), and commonly transect whole fining-upward cycles (several 10s of meters).

The faults with tens to hundreds of meters of displacement are here named large faults, which may offset thick heterolithic rock units dominated by fine-grain rocks. High quality outcrops of these faults are relatively rare in the study area because they are much more erodible than the surrounding rocks. For example, Fig. 7(a) shows the central part of the east-west trending Coca Fault mapped from an aerial photograph (Fig. 2c). This fault has four main strands, and its architecture is similar to other east-west oriented faults. It shows an apparent right-lateral offset of hundreds of meters. However, a main strand (Fig. 7b), which exposes principal slip surfaces, has oblique-slip indicators with mostly dip-slip indicating about 40 m of throw (Fig. 7c) based on correlated stratigraphic units on both sides of the fault zone. The fault core is 30 cm-wide, and consists of uncemented cataclasite and fine breccia. On the south side, the fault damage-zone consists of joints and sheared joints within about four meters of the main slip surface. On the north side, the sandstone beds are intensely fractured whereas the shale-rich beds show tilting consistent with the dip-slip motion (Fig. 7b).

IEL fault is another east-west oriented large fault displaying right-lateral apparent offset, which varies along strike and reaches a maximum value of 75 m (Fig. 7d). Similar to other large fault zones, the IEL fault has numerous strands that overlap and link. The boundaries of the fault damage zone were established based on the intensity of fractures observed in the adjacent sandstones. Where zonal boundaries were not accessible, we estimated the damage-zone width based on a combination of digital scanlines (on satellite images) and the morphological expression of the fault zone, which is noticeably low-relief respect to the surroundings.

Cilona et al. (2015) identified shale smearing in outcrop (Fig. 8) based on the fault exposure, and morphology along the so-called Shear Zone fault (Sage, 1971; MWH, 2009), one of the largest faults at SSFL. Another example for this class of relatively large faults is the Santa Susana Pass fault (see Fig. 1b for location) across which an oblique-slip displacement with a vertical separation of 150 m (Fig. 8c, d) can be inferred.

4.4. Dimensional parameters

4.4.1. Joints

The relationship between thickness of the sandstone units and the spacing of each of the two oldest sets of joints (NE–SW and

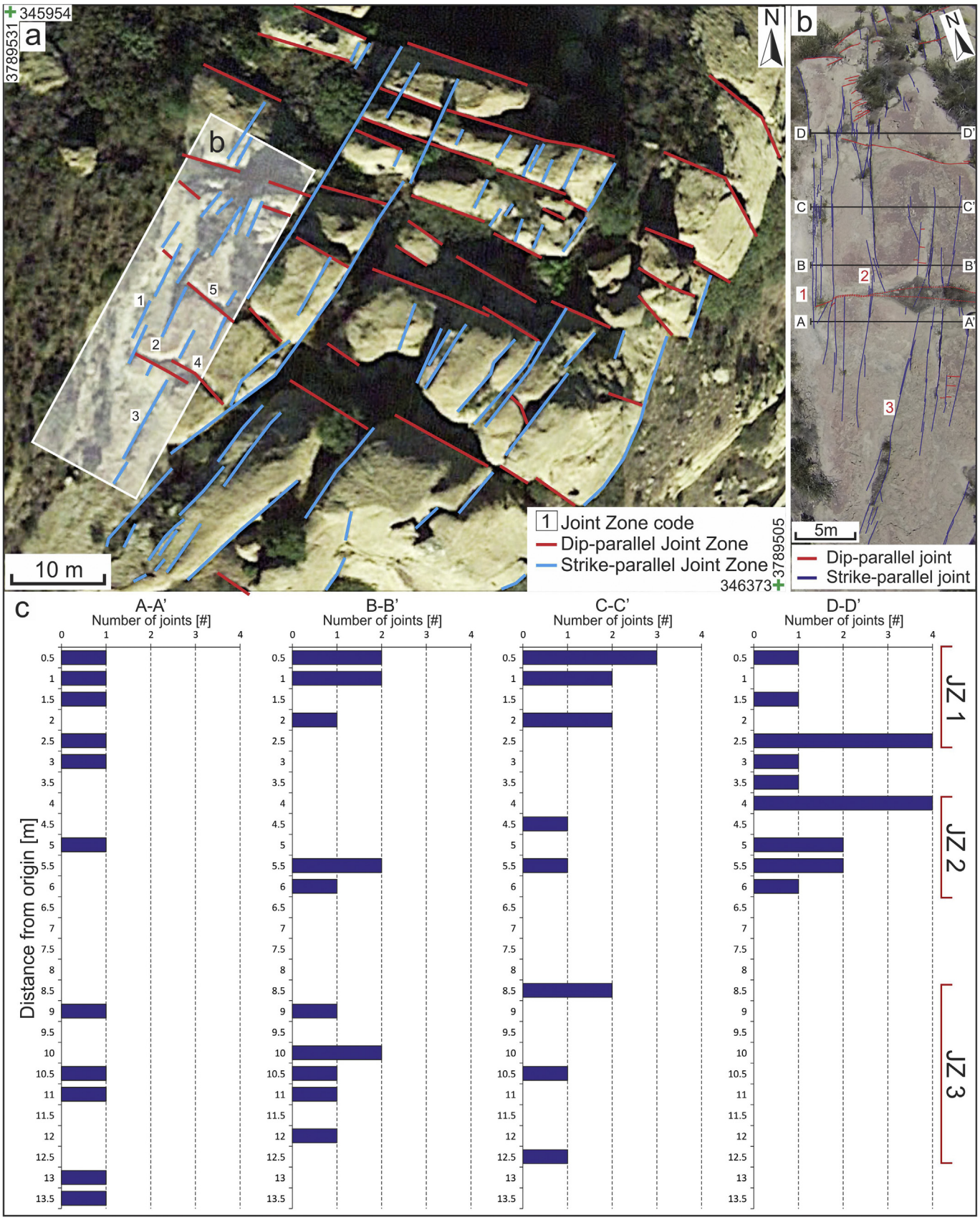

Fig. 4. a) Dip-parallel and strike-parallel joint zones network (green crosses mark the UTM 11S coordinates), location of (b) is shown by a semi-transparent polygon. b) Architecture of strike-parallel joint zones mapped from a low-altitude drone image (red numbers indicate JZs). The black lines are four digital scanlines for sampling fracture density at different locations along the joint zones. c) Joint positions along the scanlines A to D.

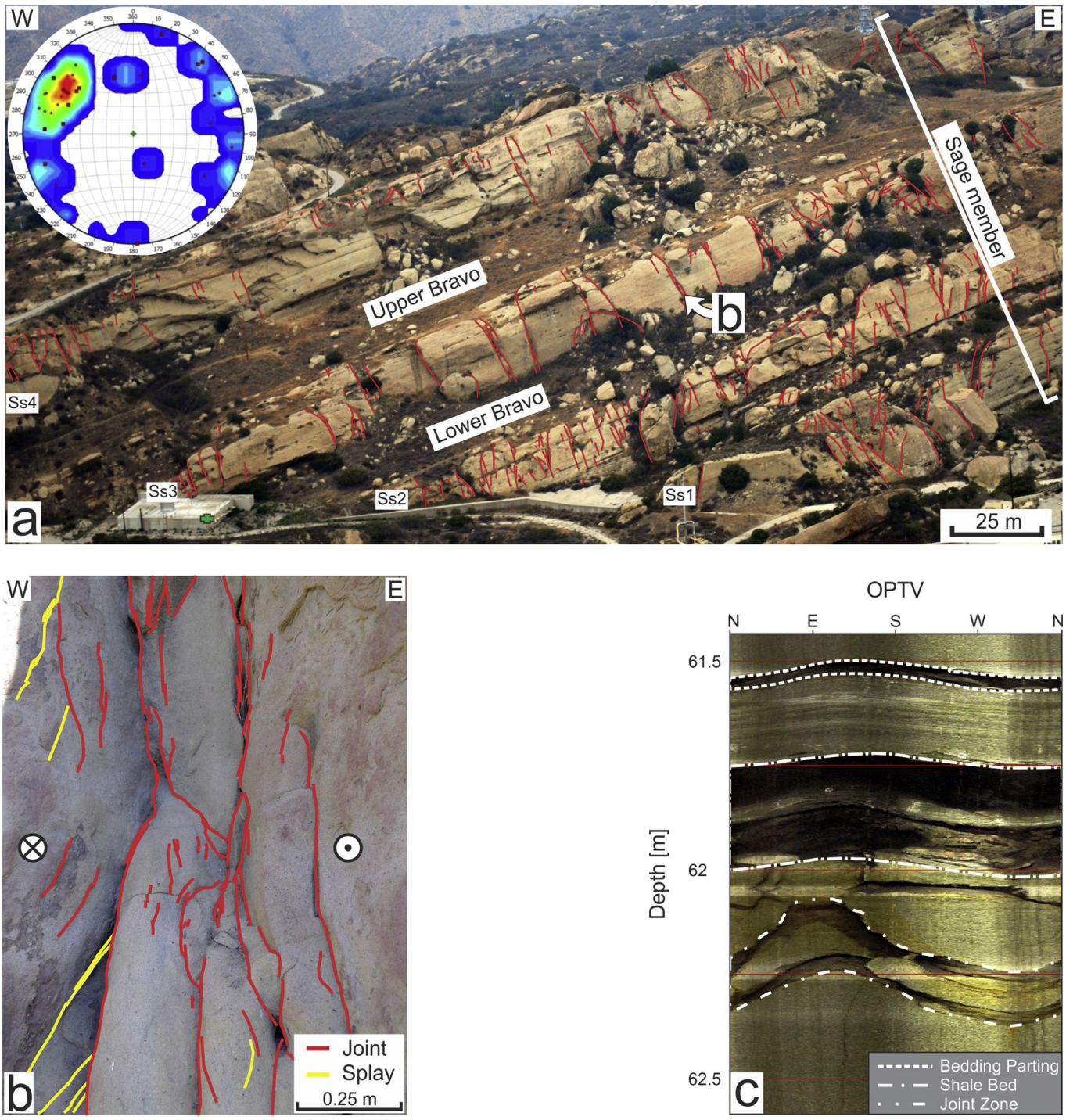

Fig. 5. a) Cross sectional view of the joint zones distribution within the sandstone intervals of the Sage member exposed north of the Coca area (UTM 11S coordinate of the green cross: 343326E; 3788688N). Joint zones mostly confined within the four sandstone units marked as Ss1 to Ss4 are shown in red, inset equal area, low hemisphere projection of the average orientation of measured joint zones (2% contour); b) Architecture of a joint zone reactivated by shear (see circles for kinematics) with multiple joints (red) and relative splays (yellow). See a for location; c) Optical Televiewer of well RD-35b showing the architecture of a joint zone at depth.

NW–SE) away from the faults was investigated to establish what we classified as the background fracture distribution. We collected scanline data along seven layers with thicknesses spanning two orders of magnitude (Fig. 9a). The results show that the spacing of the joints in each set positively correlates with the host layer thicknesses (Fig. 9b). The slope of the linear regression calculated for the plotted data (FSR, see Table 1) represents the FSI value of each set. For both sets of joints the FSI values are similar (~7.44 and ~7.96), meaning that the two sets have comparable intensities. The values of S/T and CV are displayed in Table 1. S/T for the NE–SW set ranges from 0.11 to 0.4 with a mean value of 0.27, whereas for the NW–SE set the range is between 0.19 and 1.56 with a mean value of 0.75. The mean value of the coefficient of variation (CV) of both sets of joints is > 1 (Table 1). However, both sets have CV values < 1

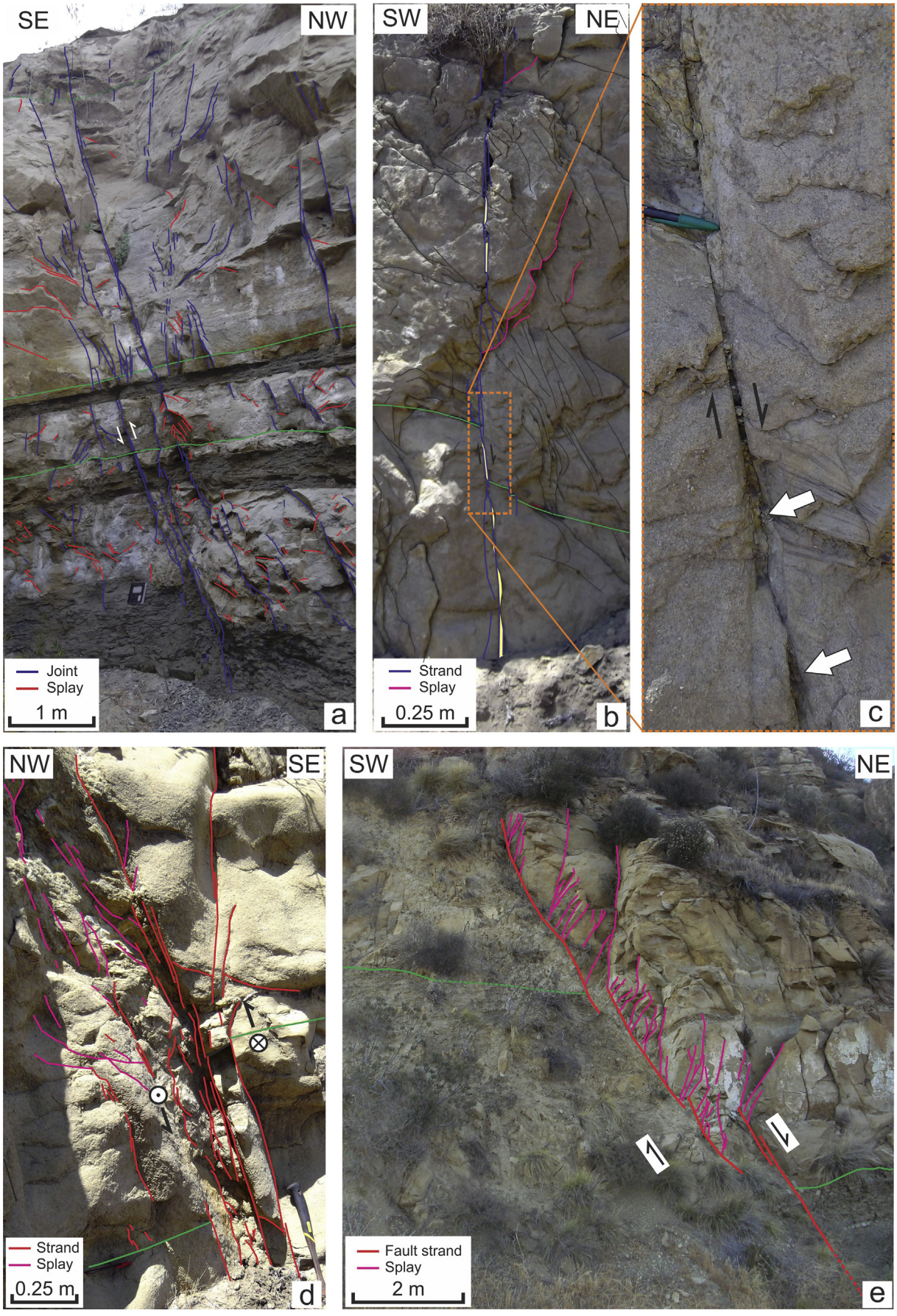
SE
NW
Joint
Splay
1 m
a
SW
NE
Strand
Splay
0.25 m
b
c
NW
SE
Strand
Splay
0.25 m
d
SW
NE
Fault strand
Splay
2 m
e

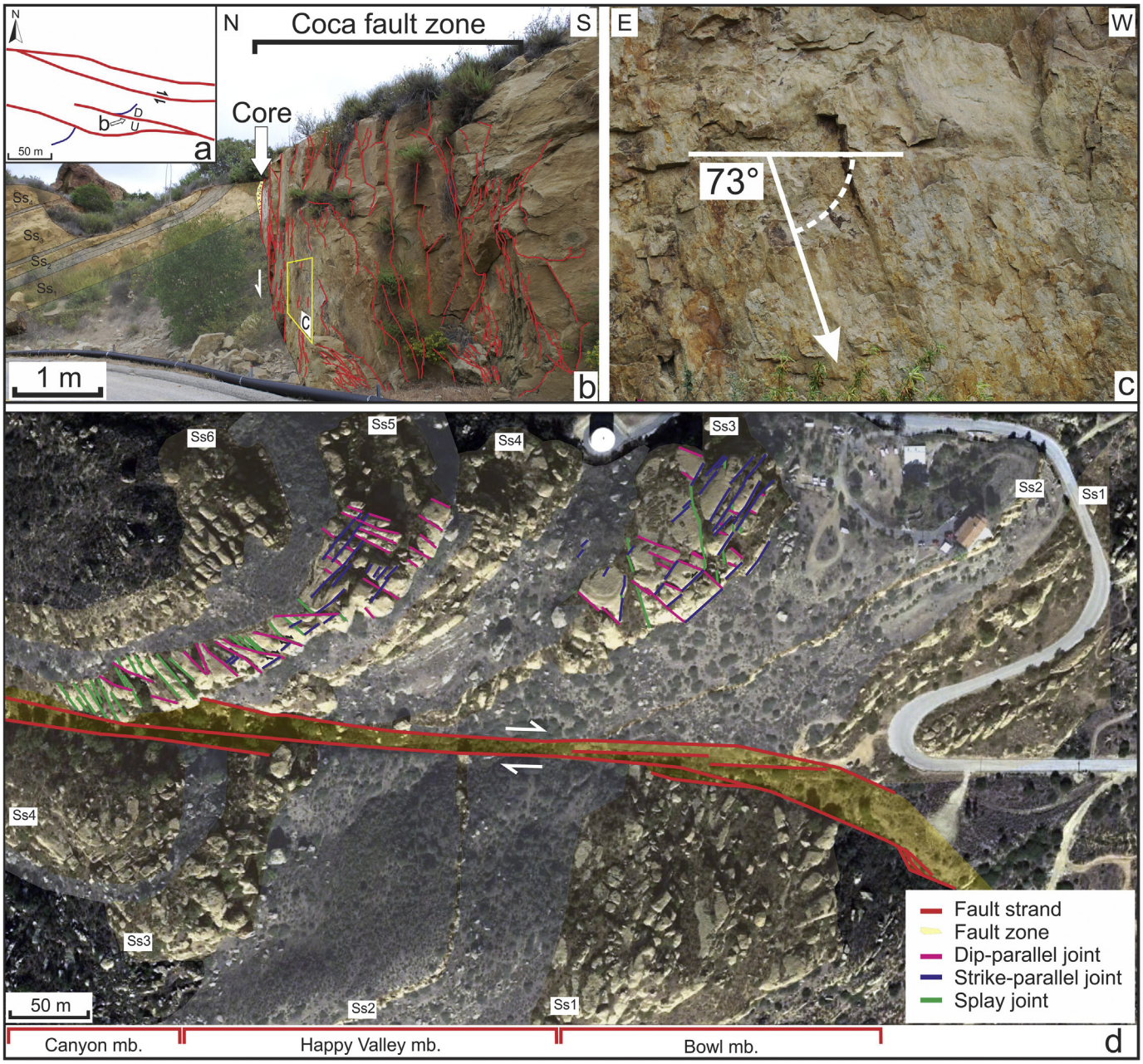

Fig. 7. a) Map of the central part of the Coca fault, fault strands are marked in red, a marker layer is represented in blue. The arrow for the location of (b), which shows a detail of the architecture of one of the fault strands (due east). Sheared joints and joints within the damage zone are shown is red, the fault core is represented by yellow infilling and geometric pattern; c) Shows the slickenside on the main slip surface. d) IEL fault zone, the faults shows a right-lateral apparent displacement and cuts across sandstones (Ss, light-brown) and shales (light-grey).

within the thinnest (0.055 m) and thickest (5 m) strata meaning that the clustering of the joints differs between these two beds.

In addition to the relationship between joint spacing and host layer thickness, mean joint spacing was also calculated (Fig. 9a). These spacing values, obtained away from faults, provide an estimate of the joint spacing within the sandstone layers at SSFL. Length distribution of background joints (for about 110 joints) is presented in Fig. 9b.

4.4.2. Fault zones

Fault zone spacing increases from one hierarchical class to the next one. In the three lowest classes we observe an increase of about one order of magnitude, whereas between the two highest classes the increase is less than the previous three (Fig. 9a).

The measured fault lengths (~2400 faults) span across four orders of magnitude (from 10^0 to 10^4 m; Fig. 10b). The comparison of

Fig. 6. Architectures of fault zones with increasing displacement values. a) Slightly sheared joint zone (blue) with 1.5 cm throw measured across a marker layer represented in green; b) Fault zone with 25 cm throw, blue lines represent slip surfaces, purple lines are splay joints. c) Close up (orange dashed rectangle) shows small pockets of fault rock pointed out by white arrows. d) Reverse fault with 60 cm throw, slip surfaces are shown in red and splay joints in purple. e) 4-m throw normal fault, offset across the green layer (top of Shale 2). Main fault segments are represented in red, splay joints in purple.

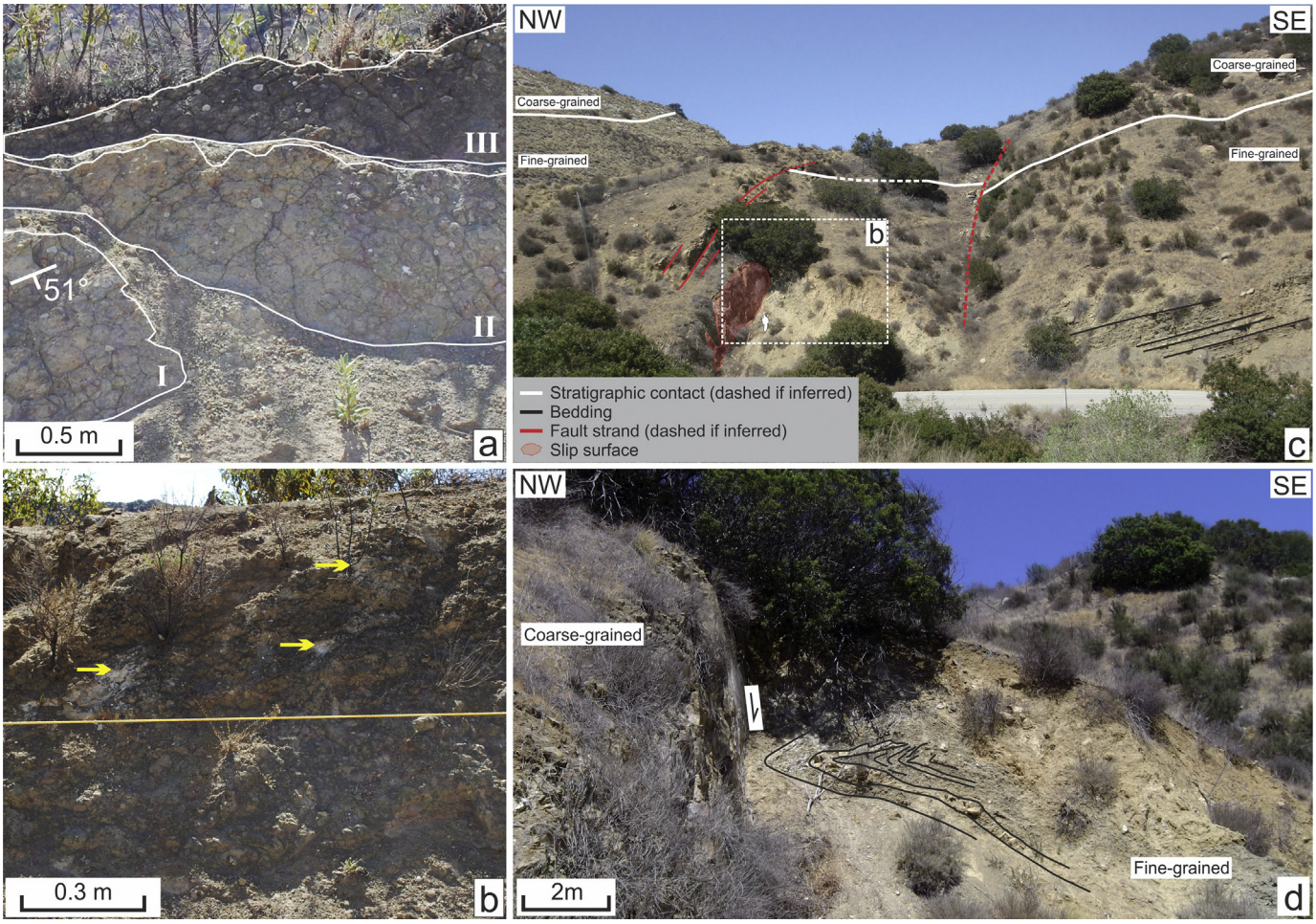

Fig. 8. Exposures of fault zones with shale-rich cores (a, b from Shear Zone Fault; c and d Santa Susana Pass Fault). A) Fine-grained unit highly bent and dipping toward the fault zone (due SE). I, II, and III represent distinct beds dipping towards the viewer and their boundaries are highlighted in white (modified from Cilona et al., 2015); b) Shale-rich fault core with carbonate veins pointed out by yellow arrows (due SE; Cilona et al., 2015); c) Offset of the coarse-grained/fine-grained contact SE side down; d) Close-up of the fault zone showing intensely folded and faulted shale beds (black).

the length distributions as a function of their general strike (i.e., E–W, NE–SW) indicates that the cumulative number of the E–W oriented faults is greater. Considering the two fault populations, each distribution has at least two slope changes on the plot, which separate portions of the dataset that are fitted by different power laws. These knees or bends do not correspond to the same length values for both orientation modes. In fact, the slope changes at greater length values for the E–W structures versus the NE–SW ones. For both fault populations the faults with lengths comprised between 10 and 100 m are the most abundant (~1300 in total).

The scaling relationships for displacement, length and width of the faults are derived from scatter plots fitted with power law relationships and R^2 values between 0.81 and 0.89 (Fig. 11). The power law relation between length and displacement indicates that the faults have lengths about one order of magnitude larger than their displacements (displacement >35 cm). In contrast, fault displacements and widths are of similar magnitude (Fig. 11b). The faults display a greater range of widths for values of displacement of less than one meter (based on 15 data points), which we interpret to result from whether particular faults nucleated across single joints or joint zones, the latter of which are almost always longer. For the width *vs.* length plot, the data follow a power law that indicates the faults have at least one order of magnitude greater length than width (Fig. 11c).

5. Discussions

In investigations with strictly structural geology objectives, the formation mechanisms of fractures and faults plus their geometry are the central issues. However, this paper has a multi-disciplinary objective: characterizing fractures and faults for an important environmental concern, which is the fate of contaminants in the groundwater system at the study area. The complexity of the problem is increased by the stratigraphic complications due to the alternating sandstone and shale composite sequences of the Chatsworth Formation. This formation is also characterized by both lateral and vertical heterogeneities (De Ros, 1998). These heterogeneities occur from centimeters to hundreds of meters scale, and may control the propagation and termination of tectonic structures of various sizes as described from other turbidite sequences (Florez-Niño et al., 2005; Gonzales and Aydin, 2008).

5.1. Joints and joint zones

The Chatsworth Formation contains two coeval orthogonal sets of joints, which are sub-perpendicular to the bedding and parallel and perpendicular to the bedding strike. This is a well-known pattern in fold and thrust belts (Caputo, 1995; Bai et al., 2002). Considering spacing within these joint sets, the reported FSI values

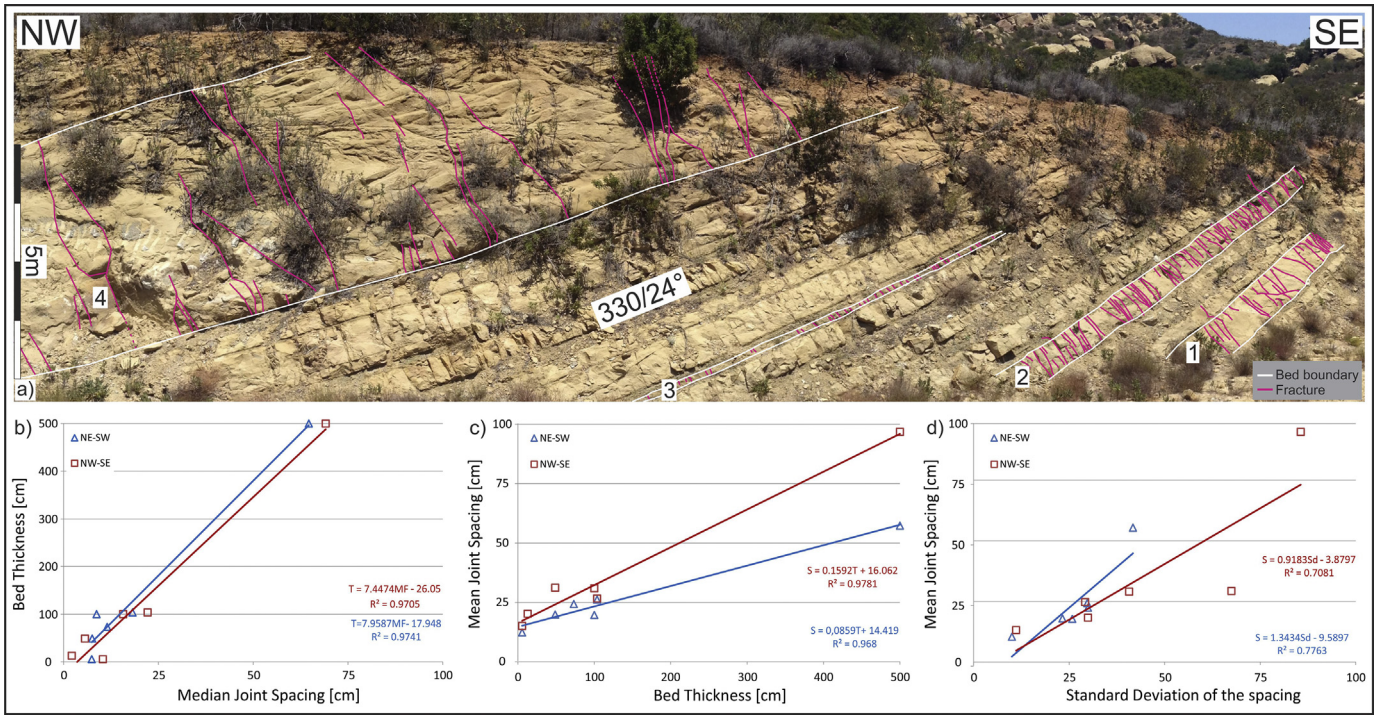

Fig. 9. a) Outcrop picture of a location where bed-parallel scanlines were performed to characterize the background distribution away from faults of the two orthogonal joint sets (UTM 11S, 344801 E, 3788415N). b) FSI; c) S/T; d) Cv.

Table 1
Compilation of the values of the four parameters calculated for the two sets of stratabound joints.

Bed number	Bed thickness [cm]	FSR		FSI		S/T		CV	
		NW	NE	NW	NE	NW	NE	NW	NE
5*	5.5	0.53	6.48	7.45	7.96	0.633	0.40	0.75	0.83
3	12.77	5.96	N/A			1.56	N/A	1.50	N/A
6*	48.77	8.68	5.70			0.25	0.25	2.18	1.19
2	73.15	N/A	6.37			N/A	0.33	N/A	1.25
1	100	6.37	11.51			0.31	0.19	1.33	1.33
7*	103.63	4.68	7.73			0.19	0.11	1.11	1.15
4	500	7.23	6.37			1.56	0.33	0.89	0.73
*data from an outcrop not shown in Fig. 9						Mean value			
N/A = bed with not sufficient amount of joints to calculate the parameter		5.58	7.36	7.45	7.96	0.75	0.27	1.29	1.08

for other tectonic joint systems are between 0.8 and 1.5 (Gross, 1993; Narr and Suppe, 1991; Rustichelli et al., 2013) and have a linear correlation between joint spacing and mechanical unit thickness (Huang and Angelier, 1989; Gross et al., 1995; Wu and Pollard, 1995; Laubach et al., 2009). In this study, we obtained greater FSI values by a factor of 5–10 for the orthogonal joint sets (Table 1). Bed thickness correlates linearly to joint spacing, but the high values of FSR and FSI indicate that the joint sets did not reach a full saturation level. Indeed, according to Wu and Pollard (1995) and Bai and Pollard (2000) fully saturated joint sets should yield to FSR and FSI values close to one.

Many of the beds analyzed (5 of 7) have Cv values > 1 (Table 1), implying that these joint populations are clustered (Gillespie et al., 1993). This interpretation is also consistent with our field observation of small-to medium-scale joint zones/clusters (Fig. 4). The joint zones (JZs) can be confined within single layers and thus have a spacing roughly proportional to the layer-thickness or they can cut across stacks of beds separated by extremely thin fine-grained interlayers or bedding partings (Fig. 5). In this latter case, the spacing of the JZs depends on the thickness of the whole fractured mechanical layer (Shackleton et al., 2005).

5.2. Fault hierarchy and evolution

The two sets of joints and joints zones are inferred to be formed before any significant tilting of the strata associated with the development of the regional anticline (Dibblee, 1992) or the monocline (Yeats, 1987). Considering that the Western Transverse Ranges was subjected to up to 90° clockwise rotation with layers tilting since early-Middle Miocene (Nicholson et al., 1994; Langenheim et al. 2011), reactivation of these joint sets as faults is to be expected (Figs. 5–8, 10, 12). We portray this reactivation as a continuous process that involved more joints or joint clusters through time and lead to some of the early faults developing into large faults in the study area (Fig. 12).

Small faults (~10 cm displacement) are very discontinuous because they nucleate from joints or poorly developed joint zones that are inherently limited in size. As soon as the fault displacement reaches a few tens of centimeters, linkage of the neighboring fault segments dominates the faulting process (Cartwright et al., 1995; de Joussineau and Aydin, 2007). At this stage, discontinuous patches of proto-fault rock form primarily at stepovers (Fig. 6c). The presence of fault rock enhances the localization of slip and the

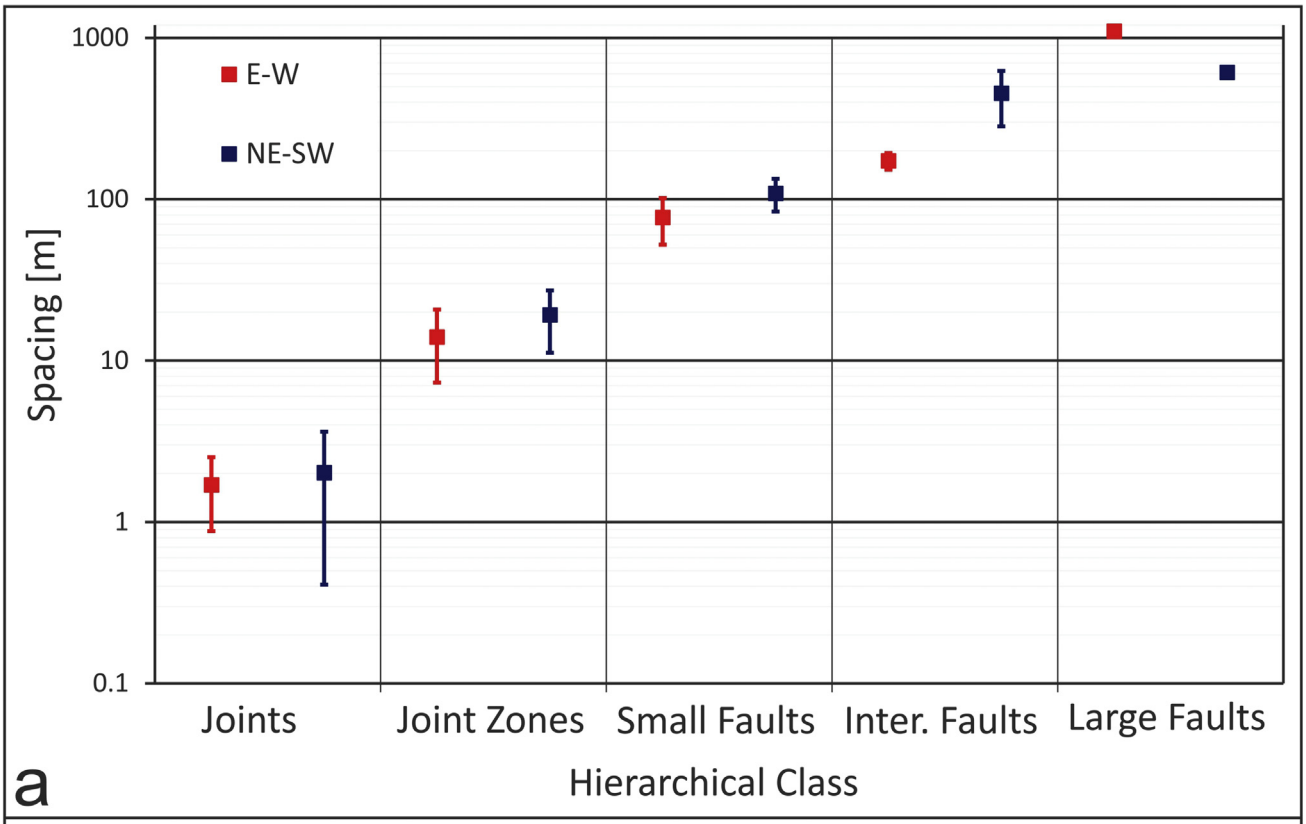
1000
100
10
1
0.1
E-W
NE-SW
Spacing [m]
Joints
Joint Zones
Small Faults
Inter. Faults
Large Faults
Hierarchical Class
a

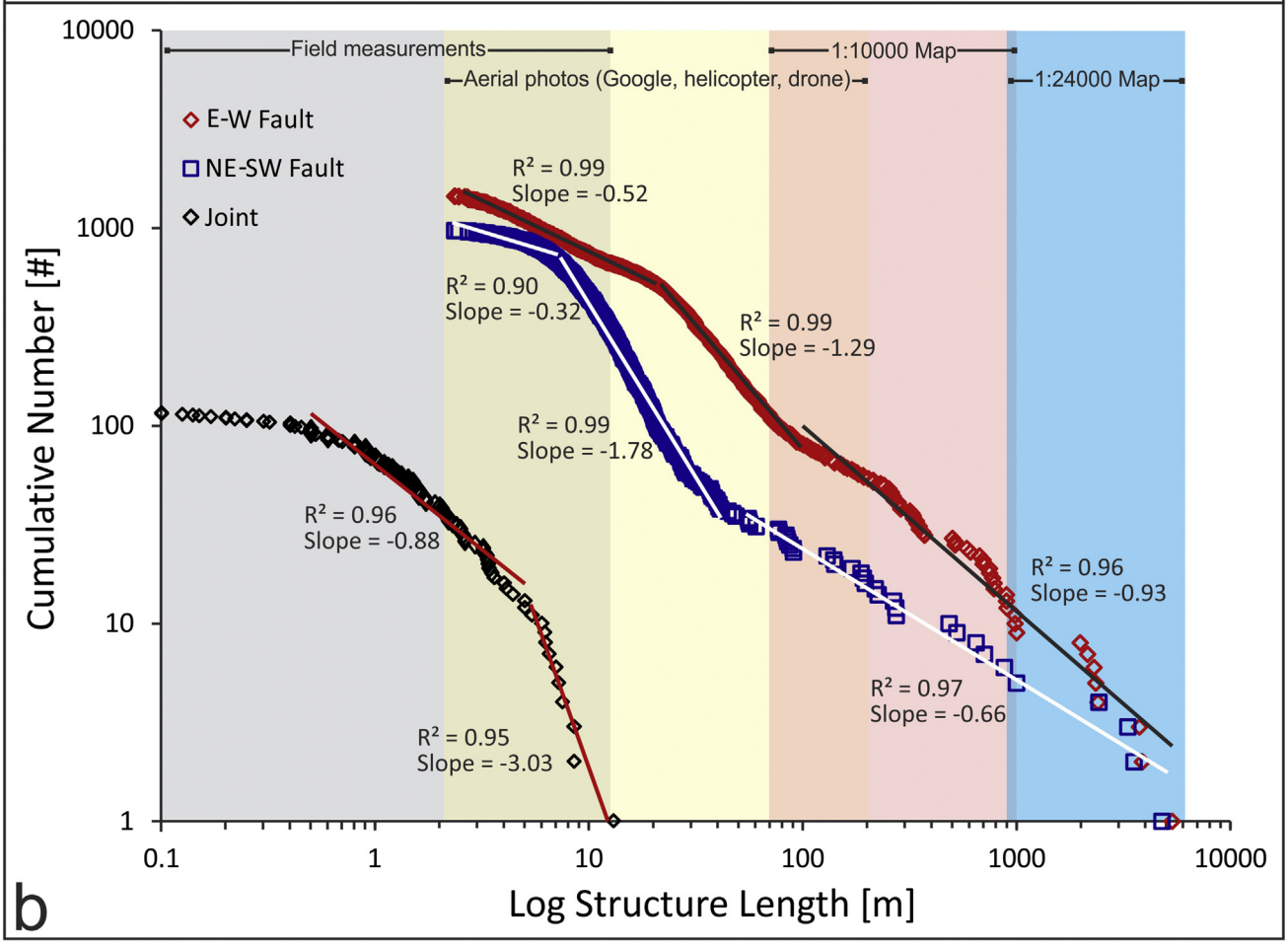
10000
1000
100
10
1
0.1
1
10
100
1000
10000
Field measurements
Aerial photos (Google, helicopter, drone)
1:10000 Map
1:24000 Map
E-W Fault
NE-SW Fault
Joint
R² = 0.99
Slope = -0.52
R² = 0.90
Slope = -0.32
R² = 0.99
Slope = -1.29
R² = 0.99
Slope = -1.78
R² = 0.96
Slope = -0.88
R² = 0.96
Slope = -0.93
R² = 0.97
Slope = -0.66
R² = 0.95
Slope = -3.03
Cumulative Number [#]
Log Structure Length [m]
b

growth of the fault zones. Intermediate fault zones with more than a few to several meters of displacements have narrow and relatively continuous fault cores and the boundary fault core/damage zone is sharper (Fig. 7d).

As deformation progressed, continuing linkage and displacement accumulation created larger faults with wider zones, offset of sequences of sedimentary layers, and formation of multiple strands (Figs. 7 and 12). After the accumulation of this history of brittle deformation, the largest faults are the least abundant and bound large rock volumes within which smaller and more numerous faults are present as characterized quantitatively in this study. This scale-invariant system keeps occurring down to the joints that represent the smallest and, of course, most abundant structures at SSFL (Fig. 12c). Table 2 summarizes structural and stratigraphic data of SSFL.

Following the work performed by Florez-Niño et al. (2005), we propose a correlation between the spacing of different fracture hierarchies (Fig. 10a) and thickness of the host stratigraphic intervals (Fig. 2a). The length distributions of both sets of fault zones show two sharp breaks of the slope (Fig. 10b). The segments between two knees have similar slopes and are fitted by power laws. Thus, the overall length distribution of these faults can be defined as multifractal. Previous authors have attributed the multifractal properties of fault networks to the existence of distinct sets (Jiandong et al., 1999) or to different faulting mechanisms (Berkowitz and Hadad, 1997). According to Cowie et al. (1995), the multifractal properties are characteristic of fault networks that reached a mature stage of development and fault coalescence and linkage dominated over nucleation. de Joussineau and Aydin (2007) suggested that the contrasting length properties of joints, sheared joints and small faults reflect different stages of the evolution of these structures and the final fault networks. Short fractures and faults keep forming during all stages of network evolution (Fig. 12), whereas longer faults by definition represent a more mature stage by progressive linkage (Cartwright et al., 1995; de Joussineau and Aydin, 2007). The interpretation proposed by these authors may explain the presence of the two breaks corresponding to 50 and 70 m of length. However, the knees at 10 m (NE–SW set) and 30 m (E–W set) in the present data may be due to an interplay of the thickness of fining-upward cycles, which influences the heights of the faults, and the truncation fault length related to mapping resolution.

The fault length *vs.* displacement data (for displacement > 0.3 m; Fig. 11a) show a good correlation with length being one order of magnitude larger than fault displacement. A broad compilation of literature data on siliciclastic rocks (Torabi and Berg, 2011) indicates that fault length should be expected to be on the order of, or three orders of magnitude larger than fault displacement. Whereas, based on theoretical reasoning, length should be two orders of magnitude greater than displacement (Scholz, 2002), which is consistent with the power law interpolation for our complete dataset. Nicol et al. (2010) suggested that the presence of a wide range of slopes in the power laws may depend on the fact that the slope changes at different stages of the fault system evolution.

The fault width *vs.* displacement plot (Fig. 11b) follows a linear trend with displacement being larger than width by a factor of two. This ratio falls within the range reported from other field and theoretical studies (Scholz, 2002; Torabi and Berg, 2011). The results presented in this paper appear to be less scattered beyond 0.3 m displacement. The greater scattering in displacements <0.3 m can be a consequence of a number of phenomena. For example: (i) the shearing of joint zones that produce relatively wide faults with little displacement; or (ii) linkage by extensional jogs, which can drastically increase the width of a fault zone (Kim et al., 2004; de Joussineau and Aydin, 2007; Tondi et al., 2012).

Width/length values of the faults zones in the study area follow a linear trend with the fault lengths being almost two orders of magnitude larger than the fault widths for a range of displacements. These results are consistent with fault width/fault displacement ratios from literature (Scholz, 2002). Scatter was observed also in this distribution, and previous studies of siliciclastic rocks suggest that the scatter can be ascribed to lithological variation in the host rock (Knott et al., 1996; Sperrevik et al., 2002). However, it is not clear if this explanation applies at SSFL because a systematic characterization of the host rock heterogeneity has not been conducted, so their impact on fault attributes are unknown.

5.3. The effect of faults and fractures on fluid flow and contaminant transport

Here we address the use of structural geological insights for interpreting hydrogeological evidence for a dense network of interconnected fractures and the role of faults in the larger scale hydrogeology. At SSFL, groundwater flow occurs almost entirely in the fractures because the rock matrix has low permeability, as shown by tests performed on intact rock plugs by Hurley and Parker (2007), Hurley et al. (2007a, b; Fig. 14). Results from straddle packer hydraulic tests (Quinn et al., 2015), flexible liner transmissivity profiling (e.g. FLUTe T-profiling explained in Keller et al., 2014) and high-resolution temperature profiling using an active line source (ALS in Pehme et al., 2013) show that hydraulically active fractures (i.e., bedding partings and sub-vertical joints) occur nearly everywhere at SSFL.

For the hydraulic connectivity, we discuss four lines of hydrogeological evidence: the distribution of contaminants (Cherry et al., 2009; Sterling et al., 2005), high resolution head profiles showing zones of measurable head loss and no head loss (Meyer et al., 2014), hydraulic conductivity tests in single boreholes (Quinn et al., 2012, 2015), and large scale pumping tests with observation wells (Reiners and Johnson, 2009; Alegre et al., submitted). These hydrogeological evidences indicate that the fracture network has strong connectivity in all directions, including the vertical one, even though the bedding dips ~30° to NW and low-conductivity lithologies such as siltstones, shales and well-cemented sandstones are present. This outcome implies that the fracture network must provide vertical or nearly vertical hydraulic pathways across low-hydraulic conductivity lithologies.

The contaminant distributions, of which trichloroethylene (TCE) is the most important, indicate a deep density driven flow of TCE. The migration of this contaminant in the groundwater system started decades ago at numerous release locations and took place as dense non-aqueous liquids (DNAPLs). Today, DNAPL reached a penetration depths up to hundreds of meters at some locations (Cherry et al., 2009), because of its strong propensity to enter and flow in fractures, even with small apertures (Kueper and McWhorter, 1991). Moreover, TCE distribution in the rock indicates that there was strong vertical migration with only minimal shunting of the DNAPL down dip along the bedding.

As corroborating evidence for strong vertical connectivity, the many vertical profiles of hydraulic head, measured using high

Fig. 10. a) Scatter plot showing the characteristic spacing of different classes of fractures (joints and joint zones) and fault zone (small, intermediate, and large). The error bars represent the standard deviation. b) Cumulative number of fracture lengths obtained from field measurements (joints) and image analysis of multi-scale maps. Close to each line segment of the distribution curves we reported the coefficient of determination and the slope of the negative power-law.

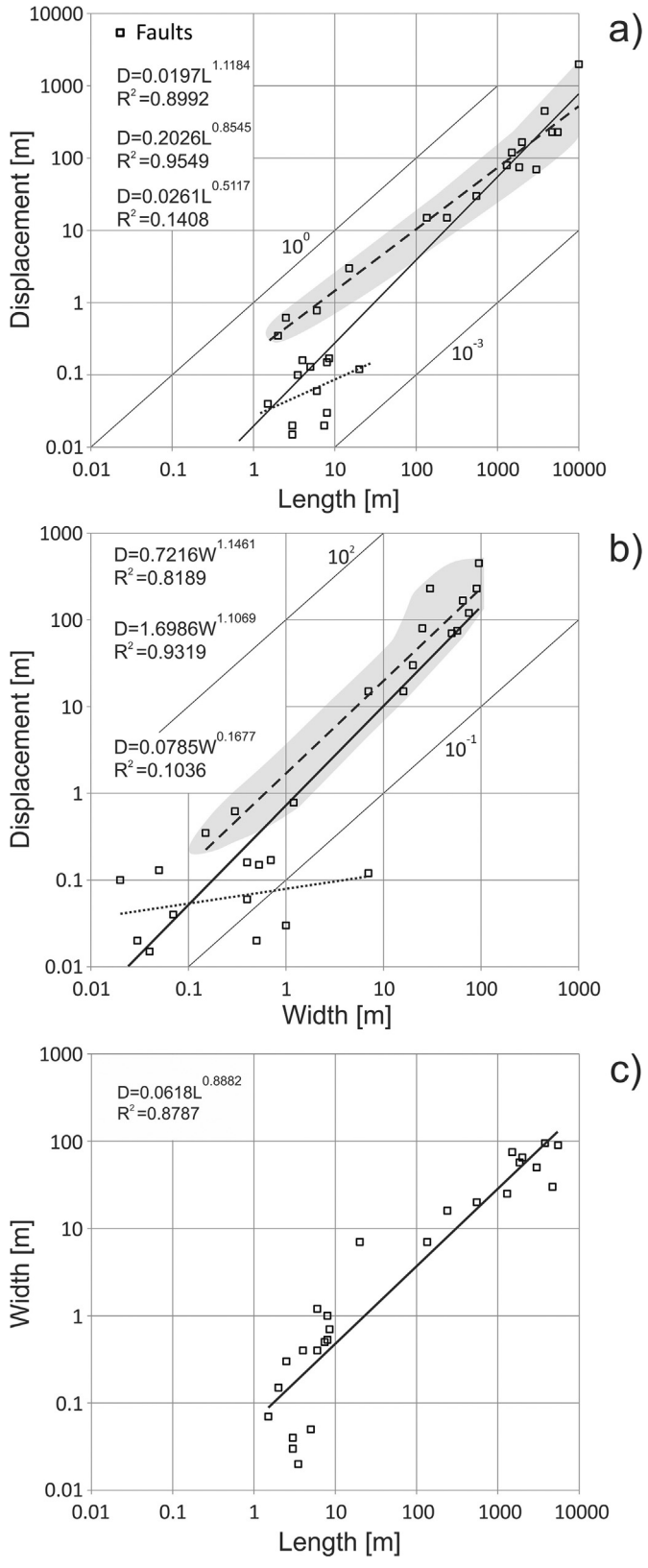

Fig. 11. Log–log plots correlating different fault parameters. a) Displacement vs. length (27 data), solid line the best-fit power-law interpolation for all data, dotter line best fit for displacement <0.3 m, and dashed line best fit for displacement >0.3 m; b) Displacement vs. width (27 data), solid line the best-fit power-law interpolation for all data, dotter line best fit for displacement <0.3 m, and dashed line best fit for displacement >0.3 m; c) Width vs. length (26 data), solid line is the best-fit power-law interpolation.

resolution multilevel monitoring systems in each borehole show little or no vertical head gradient throughout the upper few hundred meters of the Chatsworth Formation except across a few thin zones (Meyer et al., 2014), which indicates strong vertical hydraulic connectivity nearly everywhere.

Our structural analysis of joints and faults shows that the observed strong vertical connectivity is because multiple joint sets provide vertical pathways for downward flow connecting bedding partings. In other words, stratabound joints with their heights controlled by bed thickness (Fig. 9) and most importantly their linkages provide vertical connectivity within single fractured units. Additionally, sheared joints/joint zones and small faults cut across mechanical interfaces and fine-grained laminae that would otherwise hamper the flow (Fig. 10). For example, Fig. 6a shows a slightly sheared joint cutting across thin shale beds, this field observation is consistent with depth profiles of TCE showing contamination across several shale beds (e.g., Sterling et al., 2005).

At SSFL, the characteristic head profiles with only a few abrupt inflections, where the resistance to flow is strong (as indicated by large vertical components of the hydraulic gradient), are consistent with the sheared joints/joint sets and small faults commonly providing hydraulic connections across vertical dimensions of tens of meters. Thin zones (<5 m thick) with strong resistance to vertical flow represent the exception and not the rule, meaning these head loss zones are not predictable on lithology alone.

The opportunity of estimating the contribution of fractures on flow is given by the response of the bedrock to long-term pumping tests, performed by Reiners and Johnson (2009). These authors calculated bedrock bulk hydraulic conductivity at several locations with SSFL. Whereas, Hurley and Parker (2007), Hurley et al. (2007a, b) sampled of the same units (45 plugs) and laboratory tested them to measure the hydraulic conductivity of the unfractured rocks. The bulk hydraulic conductivities from pumping tests are about two orders of magnitude higher than the laboratory measurements (Fig. 14), suggesting that fractures increase the hydraulic conductivity by two orders of magnitude.

Consideration of the hydraulic head distribution in the three-dimensional context shows areas with large lateral head differentials indicative of large horizontal components of the hydraulic gradient caused by faults. Fig. 13a (modified from MWH, 2009) shows an example in the eastern quadrant of the site where there is a distinct head drop across the so-called Shear Zone fault. Cilona et al. (2015) attributed this head differential to a shale-rich core in the fault (~35%; see Fig. 8a). Smearing of shales produced two-to-three orders of magnitude hydraulic conductivity reduction in the fault core relative to the hosting sandstones (Cilona et al., 2015). Such low hydraulic conductivity in the core is consistent along the fault which in one area shows a cross-fault head differential up to 75 m (Fig. 13b).

In the northeast part of the site, the Shear Zone Fault represents the northeastern boundary of a major contaminant plume, which extends parallel to the fault on its southeast side (Cherry et al., 2009). The lack of transverse spreading plume across the fault is consistent with the low hydraulic conductivity in the fault core that minimizes cross-fault flow and promotes fault-parallel flow. However, examination of the head distribution across the site shows areas where faults do not show head differentials. For example, cross-section B–B′ (Fig. 13c; after MWH, 2009) crosses two of the E–W trending faults (IEL and Happy Valley faults). Here the network of monitoring wells shows no substantial head differences across the faults indicating that they are not impeding large-scale cross-fault groundwater flow (i.e. these faults appear to show similar bulk K and contribute to the interconnected fracture network in this area). This outcome is consistent with the architecture that we described for one of the strands of the Coca Fault

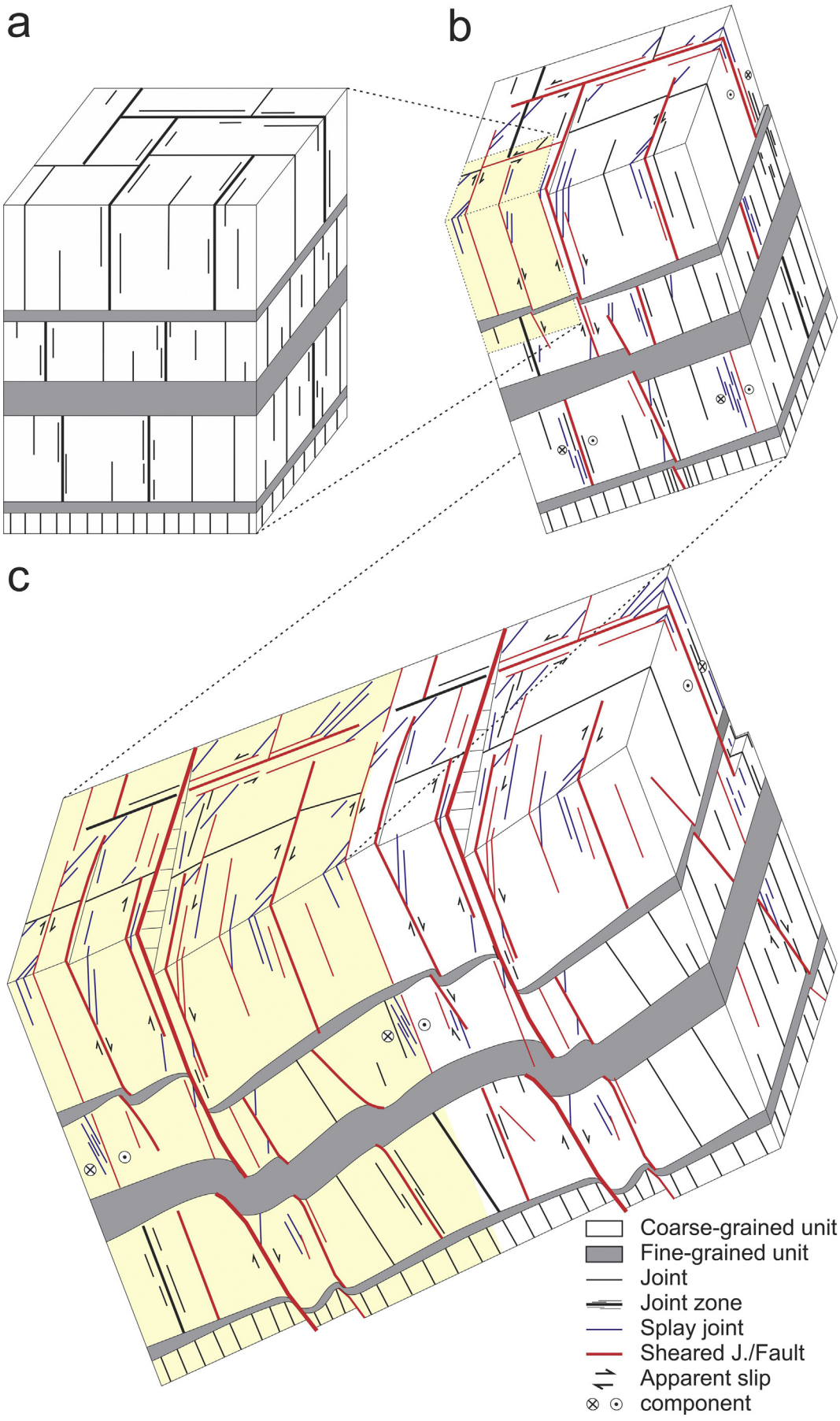
a
b
c
Coarse-grained unit
Fine-grained unit
Joint
Joint zone
Splay joint
Sheared J./Fault
Apparent slip
component

Table 2
Relationship between Fracture and Stratigraphic Hierarchies. Mean fracture spacing (S) from obtained from Fig. 9b, estimated thickness (T) obtained from Fig. 2.

Fracture hierarchy	Mean spacing, [m]	Confining stratigraphic interval	Estimated thickness, [m]	Ratio T/S
Joint	2	Single Bed	N/A	7.5
Joint Zone/Incip. Fault	17	Bed set (fractured unit)	25	1.5
Small Fault	95	Single Cycle	80	0.85
Intermediate Fault	300	Sequences (Ss1 and Ss2)	560	1.9
Large Fault	850	Composite Sequence (Chatsworth Fm.)	1200	1.4

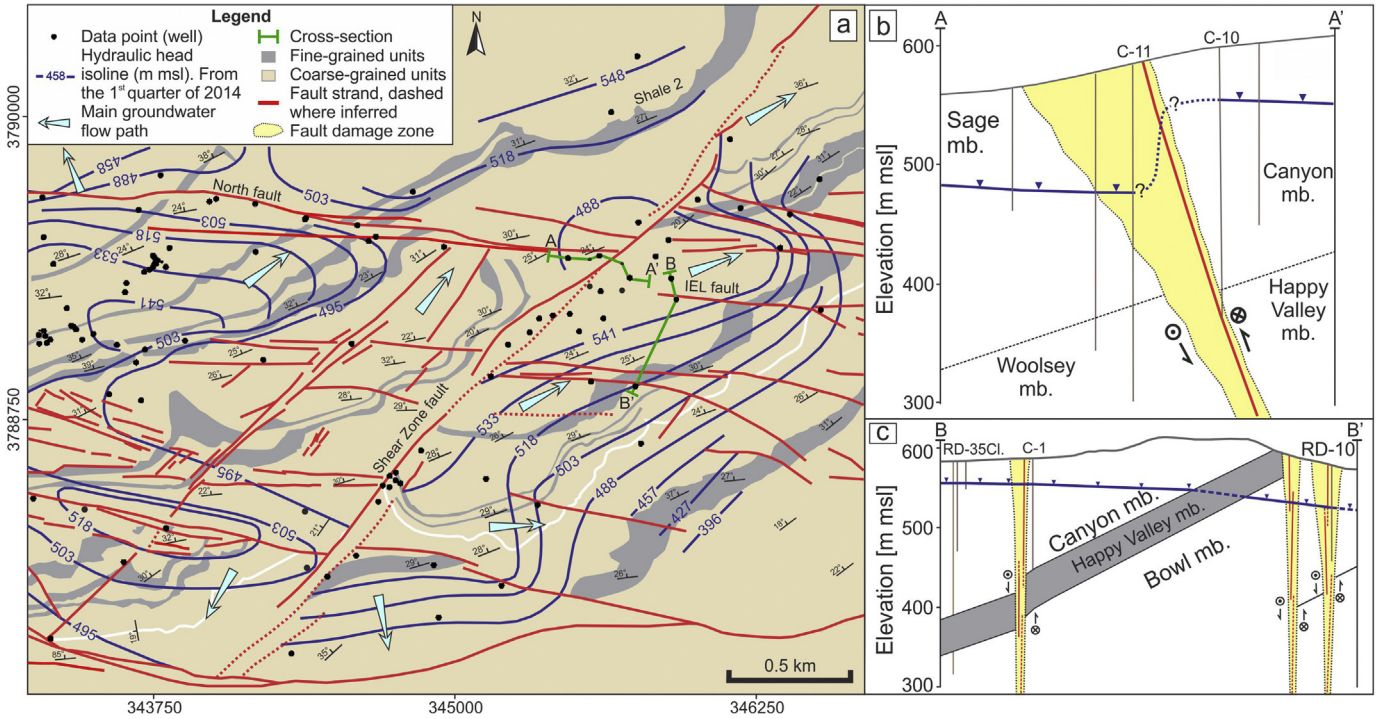

Fig. 13. a) Hydrogeological map of the Santa Susana Field Laboratory (data source MWH, 2014; modified from Cilona et al., 2015). The hydraulic head elevation (blue lines) and well locations (solid circles) are shown. b) Schematic cross-section A–A′ in (a), showing the hydraulic head drop recorded in five wells located along an approximately E–W direction on either side of the Shear Zone fault (modified from MWH, 2009). c) Schematic cross-section B–B′ in (a), showing an almost continuous hydraulic profile recorded at five wells located along an approximately N–S direction. The section crosses IEL and Happy Valley faults, respectively (modified from MWH, 2009).

(Fig. 7b) where a thin uncemented fault core is surrounded by a few meter wide fractured damage zone.

Jourde et al. (2002) modelled the permeability of faults with similar architecture and displacement ranging from 6 to 150 m. They found a positive correlation of fault-parallel permeability and slope magnitude and a negative correlation of fault-normal permeability and slip. However, in the study area, faults with displacement of ~150 m are nevertheless highly segmented with their thin cores not sufficiently continuous to provide a continuous low-permeability zone along strike.

This multidisciplinary study provides correlations of fault and fracture dimensional parameters consistent for both structural geology and hydrogeologic frameworks. These correlations may be used to build realistic Discrete Fracture Network models of the fault and fracture system at SSFL. In turn, these models may be used to simulate groundwater flow and contaminant transport improving existing simulations based on a simplified geometric representation of the fracture network (Parker et al., 2010, 2012).

6. Conclusions

This outcrop-based structural analysis of joints and the multi-scale network of faults crosscutting the sandstone/shale sequence exposed throughout SSFL and vicinity, provides geological explanations for the important hydrogeologic characteristics observed only from boreholes and interpretations. The rock has a high frequency of hydraulically active fractures consisting of a combination of joints and the bedding partings dipping 30° to the NW. Vertical boreholes provided information about the bedding parallel fractures but not much about the sub-vertical features. This structural analysis focused on sub-vertical structures to support and explain the hydrogeological observations.

The oldest structures in the study area are two sets of orthogonal bed-perpendicular joints and joint zones oriented NE–SW and NW–SE. These are referred to as the background fractures. Consistent with the previous results in the literature, the spacing of these fractures is strongly controlled by the thickness of host beds

Fig. 12. Schematic block diagram of fault nucleation and evolution. a) Precursor joint formation prior to tilting and rotation about a vertical axis of the rock mass; b) development of small to intermediate oblique-slip faults that reactivated pre-existing joints during tilting and vertical axis rotation; and c) continued fault initiation, growth and displacement creating large faults, new faults and a greater abundance of splay fractures.

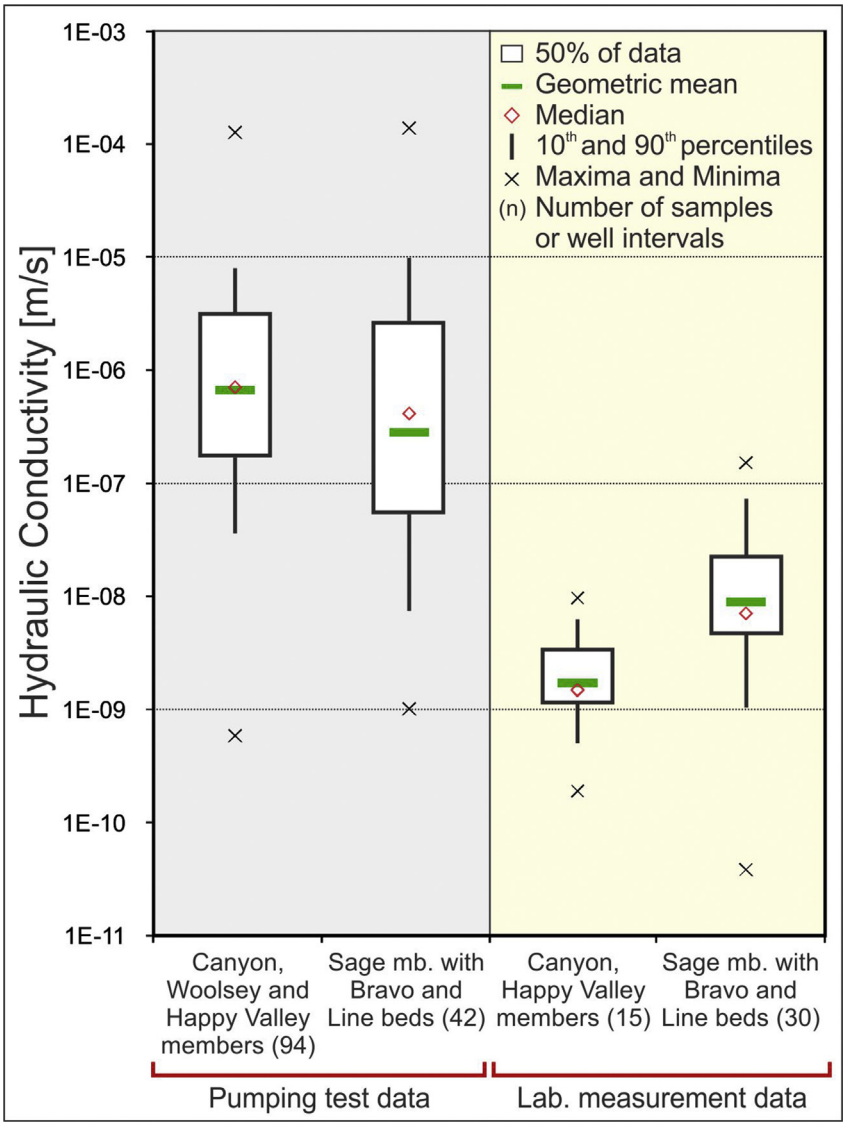

Fig. 14. Box-and-whisker plot of the hydraulic conductivity of two sandstone-dominated units of the Chatsworth Formation. The plot compares two different datasets: one obtained by well pumping tests (grey shading; data source Reiners and Johnson, 2009) and another from direct laboratory measurements on nominally unfractured samples (yellow shading; data source Hurley and Parker, 2007; Hurley et al. 2007a, b).

and/or fractured units, influencing where vertical flow is restricted creating aquitard layers and anisotropy.

Due to the interplay of a regional tilting of the strata toward the NW and the rotation of the Western Transverse Ranges block, both joints and joint zone were subjected to progressive shearing. This shearing induced the formation of various generations of splay joints, linkage of neighboring sheared structures and eventually the development of two main populations of faults oriented primarily NE–SW and ESE-WNW. To this end, we established a hierarchy of fault zones based on their displacements from millimeter to kilometer scale, which is associated with progressively increasing complex architecture. Both extent and propagation of the faults in different hierarchical classes are thought to be strongly influenced by multi-scale depositional and older structural heterogeneities that are typical of turbidite sequences and can be summarized as follows.

1. Each hierarchical class has its own characteristic value of spacing. Generally, this value varies about one order of magnitude from one class to the next.
2. Both fault populations have a multi-fractal length distribution ranging over four orders of magnitude. The trends are characterized by linear segments that can be fit by power law distributions. Other dimensional parameters such as width and spacing are consistent with the data previously published for similar rock types.

Fault architecture was used to explain the two types of hydraulic behaviors shown by hydraulic monitoring across faults. Faults characterized by shale smearing provide strong resistance to fault-perpendicular flow due low hydraulic conductivity in their shale-rich fault cores. In contrast the fault zones mainly confined within the sandstone layers do not show enhanced resistance to cross-fault flow. However, in some areas, these faults may enhance fault-parallel groundwater flow due to extensive (10s of m-wide) strike-parallel damage zones.

The structural analysis of the hierarchy of joints and fault zones provides evidence consistent with the hydrogeologic data. The abundance of sheared joint zones and relatively small faults cutting

across lithologic units causes shale and siltstone beds with small rock matrix permeability to exhibit strong vertical hydraulic connectivity and substantial hydraulic conductivity with distinct zones of head loss across faults and beds. The rock matrix hydraulic conductivity measured previously on small cylindrical plugs (Hurley and Parker, 2007; Hurley et al. 2007a, b) show values about two orders of magnitude smaller than the bulk fractured rock hydraulic conductivity determined by Reiners and Johnson (2009) using large-scale, long-term pumping tests and also single-hole hydraulic tests that reflect the effects of the structural processes.

Acknowledgments

This work was supported by a grant from Boeing Company through University of Guelph. We benefitted from a close collaboration with Dr. N. Johnson and R. Andrachek from MWH Americas Inc.. Logistical support and participation of the site owner, the Boeing Company and the project manager, M. Bower, is appreciated. We wish to thank E.T. Vander Velde, and Dr. G. Hazelton for the help provided during the field campaigns. A. C. thanks Dr. C. Di Celma for the discussions about sequence stratigraphy, and all the members of the Stanford Rock Fracture Project for their inputs. We thank S. Laubach and A. Nicol for their reviews and the associated editor William Dunne for his thorough comments that greatly improved the narrative of this paper.

Appendix A. Supplementary data

Supplementary data related to this article can be found at http://dx.doi.org/10.1016/j.jsg.2016.02.003.

References

Allègre, V., Brodsky, E.E., Xue, L., Nale, S.M., Parker, B.L., Cherry, J.A., 2016. Using earth-tide induced water pressure changes to measure in-situ permeability: a comparison with long-term pumping tests. Water Resour. Res. (submitted).
Aydin, A., Eyal, Y., 2002. Anatomy of a normal fault with shale smear: implications for fault seal. AAPG Bull. 86 (8), 1367–1381.
Aydin, A., 2014. Failure modes of shales and their implications for natural and man-made fracture assemblages. AAPG Bull. 98 (11), 2391–2409.
Aydin, A., 2000. Fractures, faults and hydrocarbon migration and flow. Mar. Petrol. Geol. 17 (7), 797–814.
Aydin, A., de Joussineau, G., 2014. The relationship between normal and strike-slip faults in valley of Fire State Park, Nevada, and its implications for stress rotation and partitioning of deformation in the east-central basin and range. J. Struct. Geol. 63, 12–26.
Bai, T., Pollard, D.D., 2000. Closely spaced fractures in layered rocks: initiation mechanism and propagation kinematics. J. Struct. Geol. 22 (10), 1409–1425.
Bai, T., Maerten, L., Gross, M.R., Aydin, A., 2002. Orthogonal cross joints: do they imply a regional stress rotation? J. Struct. Geol. 24 (1), 77–88.
Bai, T., Pollard, D.D., Gao, H., 2000. Explanation for fracture spacing in layered materials. Nature 403 (6771), 753–756.
Bense, V.F., Person, M.A., 2006. Faults as conduit-barrier systems to fluid flow in siliciclastic sedimentary aquifers. Water Resour. Res. 42 (5).
Bense, V.F., Gleeson, T., Loveless, S.E., Bour, O., Scibek, J., 2013. Fault zone hydrogeology. Earth Sci. Rev. 127, 171–192.
Berkowitz, B., Hadad, A., 1997. Fractal and multifractal measures of natural and synthetic fracture networks. J. Geophys. Res. Solid Earth (1978–2012) 102 (B6), 12205–12218.
Bertotti, G., Hardenbol, N., Taal-van Koppen, J.K., Luthi, S.M., 2007. Toward a quantitative definition of mechanical units: new techniques and results from an outcropping deep-water turbidite succession (Tanqua-Karoo Basin, South Africa). AAPG Bull. 91 (8), 1085–1098.
Caputo, R., 1995. Evolution of orthogonal sets of coeval extension joints. Terra Nova 7 (5), 479–490.
Cartwright, J.A., Trudgill, B.D., Mansfield, C.S., 1995. Fault growth by segment linkage: an explanation for scatter in maximum displacement and trace length data from the Canyonlands Grabens of SE Utah. J. Struct. Geol. 17 (9), 1319–1326.
Cherry, J.A., David, B., McWhorter, Parker, B.L., SSFL Groundwater Advisory Panel, 2009. In: Site Conceptual Model for the Migration and Fate of Contaminants in Groundwater at the Santa Susana Field Laboratory, Simi, California (Draft). Volumes I through IV. Association with the University of Guelph, Montgomery Watson Harza, Haley and Aldrich and AquaResource Inc (December).
Childs, C., Walsh, J.J., Watterson, J., 1990. A Method for Estimation of the Density of Fault Displacements below the Limits of Seismic Resolution in Reservoir Formations. In North Sea Oil and Gas Reservoirs—II. Springer Netherlands, pp. 309–318.
Chong, K.P., Smith, J.W., 1984. Mechanical characterization of oil shale. In: Chong, K.P., Smith, J.W. (Eds.), Mechanics of Oil Shale. Elsevier, pp. 165–228.
Cilona, A., Aydin, A., Johnson, N.M., 2015. Permeability of a fault zone crosscutting a sequence of sandstones and shales and its influence on hydraulic head distribution in the Chatsworth Formation, California, USA. Hydrogeol. J. 23 (2), 405–419.
Colburn, I.P., Saul, L.E.R., Almgren, A.A., 1981. The Chatsworth Formation: a new formation name for the Upper Cretaceous strata of the Simi Hills, California. In: Link, M.H., Squires, R.L., Colburn, 1. P. (Eds.), Simi Hills Cretaceous Turbidites, Southern California, Pacific Section, Society Economic Paleontologists and Mineralogists, Fall Field Trip Guidebook, pp. 9–16.
Cooke, M.L., Simo, J.A., Underwood, C.A., Rijken, P., 2006. Mechanical stratigraphic controls on fracture patterns within carbonates and implications for groundwater flow. Sediment. Geol. 184 (3), 225–239.
Cowie, P.A., Sornette, D., Vanneste, C., 1995. Multifractal scaling properties of a growing fault population. Geophys. J. Int. 122 (2), 457–469.
Cruikshank, K.M., Aydin, A., 1995. Unweaving the joints in Entrada Sandstone, arches National Park, Utah, USA. J. Struct. Geol. 17 (3), 409–421.
Davatzes, N.C., Aydin, A., 2003. Overprinting faulting mechanisms in high porosity sandstones of SE Utah. J. Struct. Geol. 25 (11), 1795–1813.
de Joussineau, G., Aydin, A., 2007. The evolution of the damage zone with fault growth in sandstone and its multiscale characteristics. J. Geophys. Res. Solid Earth (1978–2012) 112 (B12).
de Joussineau, G., Mutlu, O., Aydin, A., Pollard, D.D., 2007. Characterization of strike-slip fault–splay relationships in sandstone. J. Struct. Geol. 29 (11), 1831–1842.
De Ros, L.F., 1998. Heterogeneous generation and evolution of diagenetic quartzarenites in the Siluro-Devonian Furnas Formation of the Paraná Basin, southern Brazil. Sediment. Geol. 116 (1), 99–128.
Di Celma, C.N., Brunt, R.L., Hodgson, D.M., Flint, S.S., Kavanagh, J.P., 2011. Spatial and temporal evolution of a permian submarine slope Channel–Levee system, Karoo Basin, South Africa. J. Sediment. Res. 81 (8), 579–599.
Dibblee, T.W., 1992. Geologic Quadrangle Maps: Los Angeles and Ventura Counties, California. Dibblee Foundation Geologic Maps. (a) Moorpark Quadrangle; (b) Simi Quadrangle; (c) Santa Susana Quadrangle; (d) Oat Mountain Quadrangle;(e) Camarillo and Newbury Park Quadrangles; (f) Thousand Oaks Quadrangle; (g) Calabasas Quadrangle; (h) Canoga Park Quadrangle; (i) Point Mugu and Triunfo Pass Quadrangles; (j) Point Dume Quadrangle; (k) Malibu Beach Quadrangle; (l) Topanga Quadrangle.
Eichhubl, P., D'Onfro, P., Aydin, A., Waters, J., McCarty, D.K., 2005. Structure, petrophysics, and diagenesis of shale entrained along a normal fault at Black Diamond Mines, California-Implications for fault seal. AAPG Bull. 89 (9), 1113–1137.
Engelder, T., Lash, G.G., Uzcátegui, R.S., 2009. Joint sets that enhance production from Middle and Upper Devonian gas shales of the Appalachian Basin. AAPG Bull. 93 (7), 857–889.
Faulkner, D.R., Jackson, C.A.L., Lunn, R.J., Schlische, R.W., Shipton, Z.K., Wibberley, C.A.J., Withjack, M.O., 2010. A review of recent developments concerning the structure, mechanics and fluid flow properties of fault zones. J. Struct. Geol. 32 (11), 1557–1575.
Flodin, E., Aydin, A., 2004. Evolution of a strike-slip fault network, Valley of Fire State Park, southern Nevada. Geol. Soc. Am. Bull. 116 (1–2), 42–59.
Florez-Niño, J.M., Aydin, A., Mavko, G., Antonellini, M., Ayaviri, A., 2005. Fault and fracture systems in a fold and thrust belt: an example from Bolivia. AAPG Bull. 89 (4), 471–493.
Gale, J.F., Laubach, S.E., Olson, J.E., Eichhubl, P., Fall, A., 2014. Natural fractures in shale: a review and new observations. AAPG Bull. 98 (11), 2165–2216.
Gillespie, P.A., Howard, C.B., Walsh, J.J., Watterson, J., 1993. Measurement and characterisation of spatial distributions of fractures. Tectonophysics 226 (1), 113–141.
Gonzales, J., Aydin, A., 2008. Structural characterization of deep-water deposits in a foreland basin, Silla Syncline (Chilean Patagonia), with applications to depositional processes. J. Struct. Geol. 30 (9), 1095–1108.
Gross, M.R., 1993. The origin and spacing of cross joints: examples from the Monterey Formation, Santa Barbara coastline, California. J. Struct. Geol. 15, 737–751.
Gross, M.R., Fischer, M.P., Engelder, T., Greenfield, R.J., 1995. Factors controlling joint spacing in interbedded sedimentary rocks: integrating numerical models with field observations from the Monterey formation, USA. Geol. Soc. Lond. Spec. Publ. 92 (1), 215–233.
Gudmundsson, A., 2011. Rock Fractures in Geological Processes. Cambridge University Press, New York.
Gudmundsson, A., Simmenes, T.H., Larsen, B., Philipp, S.L., 2010. Effects of internal structure and local stresses on fracture propagation, deflection, and arrest in fault zones. J. Struct. Geol. 32 (11), 1643–1655.
Helgeson, D.E., Aydin, A., 1991. Characteristics of joint propagation across layer interfaces in sedimentary rocks. J. Struct. Geol. 13 (8), 897–911.
Hodgson, R.A., 1961. Regional study of jointing in comb ridge–Navajo mountain area, Arizona and Utah. Bull. Am. Assoc. Petrol. Geol. 45 (1), 1–38.
Hooker, J.N., Laubach, S.E., Marrett, R., 2013. Fracture-aperture size-frequency, spatial distribution, and growth processes in strata-bounded and non-strata-bounded fractures, Cambrian Mesón Group, NW Argentina. J. Struct. Geol. 54, 54–71.
Huang, Q., Angelier, J., 1989. Fracture spacing and its relation to bed thickness. Geol. Mag. 126 (4), 355–362.

Hurley, J.C., 2003. Rock Core Investigation of DNAPL Penetration and Persistence in Fractured Sandstone. M.Sc. Thesis. University of Waterloo.
Hurley, J.C., Parker, B.L., 2007. Rock Core VOC Results for Corehole C9 (RD-84), Source Zone Characterization at the Santa Susana Field Laboratory Addendum Report No. 3. Department of Earth Sciences, University of Waterloo (June).
Hurley, J.C., Parker, B.L., Cherry, J.A., 2007a. Source Zone Characterization at the Santa Susana Field Laboratory: Rock Core VOC Results for Coreholes C1–C7. Final. Department of Earth Sciences, University of Waterloo (June).
Hurley, J.C., Chapman, S.W., Parker, B.L., 2007b. Rock Core VOC Results for Corehole C8, Source Zone Characterization at the Santa Susana Field Laboratory Addendum Report No. 1. Department of Earth Sciences, University of Waterloo (June).
Jennings, C.W., Strand, C.W., 1969, Geologic Map of California, Los Angeles Sheet (Olav P. Jenkins edition): California Division of Mines, scale 1:250,000.
Jiandong, X., Guosheng, Q., Jacobi, R.D., 1999. Fractal and multifractal properties of the spatial distribution of natural fractures—analyses and applications. Acta Geol. Sinica Engl. Ed. 73 (4), 477–487.
Jourde, H., Flodin, E.A., Aydin, A., Durlofsky, L.J., Wen, X.H., 2002. Computing permeability of fault zones in eolian sandstone from outcrop measurements. AAPG Bull. 86 (7).
Keller, C.E., Cherry, J.A., Parker, B.L., 2014. New method for continuous transmissivity profiling in fractured rock. Groundwater 52 (3), 352–367.
Kim, Y.S., Peacock, D.C., Sanderson, D.J., 2004. Fault damage zones. J. Struct. Geol. 26 (3), 503–517.
Knott, S.D., Beach, A., Brockbank, P.J., Lawson Brown, J., McCallum, J.E., Welbon, A.I., 1996. Spatial and mechanical controls on normal fault populations. J. Struct. Geol. 18 (2/3), 359–372.
Kueper, B.H., McWhorter, D.B., 1991. The behavior of dense, nonaqueous phase liquids in fractured clay and rock. Groundwater 29 (5), 716–728.
Langenheim, V.E., Wright, T.L., Okaya, D.A., Yeats, R.S., Fuis, G.S., Thygesen, K., Thybo, H., 2011. Structure of the San Fernando Valley region, California: implications for seismic hazard and tectonic history. Geosphere 7 (2), 528–572.
Laubach, S.E., Olson, J.E., Gross, M.R., 2009. Mechanical and fracture stratigraphy. AAPG Bull. 93 (11), 1413–1426.
Laubach, S.E., 1991. Fracture Patterns in Low-permeability-sandstone Gas Reservoir Rocks in the Rocky Mountain Region. Proceedings, Joint Society of Petroleum Engineers Rocky Mountain Regional Meeting/Low-permeability Reservoir Symposium, pp. 501–510. Society of Petroleum Engineers Paper 21853.
Laubach, S.E., 1992. Fracture networks in selected Cretaceous sandstones of the Green River and San Juan basins, Wyoming, New Mexico, and Colorado. In: Coalson, E.B., Brown, C.A. (Eds.), Geological Studies Relevant to Horizontal Drilling: Examples from Western North America, Rocky Mountain Association of Petroleum Geologists, pp. 61–73.
Link, M.H., Squires, R.L., Colburn, I.P., 1984. Slope and deep-sea fan facies and paleogeography of upper cretaceous Chatsworth formation, Simi Hills, California. AAPG Bull. 68 (7), 850–873.
Liu, C., Tang, C.S., Shi, B., Suo, W.B., 2013. Automatic quantification of crack patterns by image processing. Comput. Geosci. 57, 77–80.
Loomer, D., Al, T., Parker, B.L., 2009. Mineralogical Characterization of Drill Core Samples from the Santa Susana Field Laboratory, Ventura County, California (Prepared for The Boeing Company, NASA, and USDOE. July).
Mandelbrot, B.B., 1983. The Fractal Geometry of Nature, vol. 173. Macmillan.
Martel, S.J., Pollard, D.D., Segall, P., 1988. Development of simple strike-slip fault zones, Mount Abbot quadrangle, Sierra Nevada, California. Geol. Soc. Am. Bull. 100 (9), 1451–1465.
Meyer, J.R., Parker, B.L., Cherry, J.A., 2014. Characteristics of high resolution hydraulic head profiles and vertical gradients in fractured sedimentary rocks. J. Hydrol. 517, 493–507.
Montgomery, Watson, 2000. Conceptual Site Model, Movement of TCE in the Chatsworth Formation. Santa Susana Field Laboratory (April).
MWH, 2007. Geologic Characterization of the Central Santa Susana Field Laboratory. August. Prepared for The Boeing Company, August, 90pp. with 9 figures and 4 plates.
MWH, 2009. Draft Site-wide Groundwater Remedial Investigation Report Santa Susana Field Laboratory, Ventura County, California (Prepared for The Boeing Company, NASA, and U.S. DOE, December, v. I-VII).
MWH, 2014. Groundwater Monitoring Progress Report, First Quarter 2014, Santa Susana Field Laboratory, Ventura County, CA (Prepared for The Boeing Company, National Aeronautics and Space Administration, and U.S. Department of Energy, May).
Myers, R., Aydin, A., 2004. The evolution of faults formed by shearing across joint zones in sandstone. J. Struct. Geol. 26 (5), 947–966.
Narr, W., Suppe, J., 1991. Joint spacing in sedimentary rocks. J. Struct. Geol. 13 (9), 1037–1048.
Nicholson, C., Sorlien, C.C., Atwater, T., Crowell, J.C., Luyendyk, B.P., 1994. Microplate capture, rotation of the western Transverse Ranges, and initiation of the San Andreas transform as a low-angle fault system. Geology 22 (6), 491–495.
Nicol, A., Walsh, J.J., Villamor, P., Seebeck, H., Berryman, K.R., 2010. Normal fault interactions, paleoearthquakes and growth in an active rift. J. Struct. Geol. 32 (8), 1101–1113.
Ogata, K., Senger, K., Braathen, A., Tveranger, J., 2014. Fracture corridors as seal-bypass systems in siliciclastic reservoir-cap rock successions: field-based insights from the Jurassic Entrada Formation (SE Utah, USA). J. Struct. Geol. 66, 162–187.
Ortega, O.J., Marrett, R.A., Laubach, S.E., 2006. A scale-independent approach to fracture intensity and average spacing measurement. AAPG Bull. 90, 193–208.
Pehme, P.E., Parker, B.L., Cherry, J.A., Molson, J.W., Greenhouse, J.P., 2013. Enhanced detection of hydraulically active fractures by temperature profiling in lined heated bedrock boreholes. J. Hydrol. 484, 1–15.
Parker, B.L., Chapman, S.W., Cherry, J.A., 2010. Plume persistence in fractured sedimentary rock after source zone removal. Ground Water 48 (6), 799–803.
Parker, B.L., Cherry, J.A., Chapman, S.W., 2012. Discrete fracture network approach for studying contamination in fractured rock. AQUAmundi J. Water Sci. 60, 101–116.
Peacock, D.C.P., Parfitt, E.A., 2002. Active relay ramps and normal fault propagation on Kilauea Volcano, Hawaii. J. Struct. Geol. 24 (4), 729–742.
Pollard, D., Aydin, A., 1988. Progress in understanding jointing over the past century. Geol. Soc. Am. Bull. 100 (8), 1181–1204.
Quinn, P., Cherry, J.A., Parker, B.L., 2012. Hydraulic testing using a versatile straddle packer system for improved transmissivity estimation in fractured-rock boreholes. Hydrogeol. J. 20 (8), 1529–1547.
Quinn, P., Cherry, J.A., Parker, B.L., 2015a. Combined use of straddle packer testing and FLUTe profiling for hydraulic testing in fractured rock boreholes. J. Hydrol. 524, 439–454.
Quinn, P., Parker, B.L., Cherry, J.A., 2015b. Blended head analyses to reduce uncertainty in packer testing results from fractured rock boreholes. Hydrogeol. J. 1–19.
Reingers, Johnson, N.M., 2009. Bulk Hydraulic Conductivity, Santa Susana Field Laboratory, Ventura County, California, 6–1.
Rustichelli, A., Agosta, F., Tondi, E., Spina, V., 2013. Spacing and distribution of bed-perpendicular joints throughout layered, shallow-marine carbonates (Granada Basin, southern Spain). Tectonophysics 582, 188–204.
Sage Jr., O.G., 1971. Geology of the Eastern Portion of the "Chico" Formation, Simi Hills, California. Master's thesis. University of California, Santa Barbara, California, p. 109.
Scholz, C.H., 2002. The Mechanics of Earthquakes and Faulting. Cambridge University Press, Cambridge, p. 471.
Scholz, C.H., Cowie, P.A., 1990. Determination of total strain from faulting using slip measurements. Nature 346 (6287), 837–839.
Schulz-Rojahn, J., Ryan-Grigor, S., Anderson, A., 1998. Structural controls on seismic-scale carbonate cementation in hydrocarbon-bearing Jurassic fluvial and marine sandstones from Australia: a comparison. In: Morad, S. (Ed.), Carbonate Cementation in Sandstones, pp. 327–362. International Association of Sedimentologists Special Publication 26.
Shackleton, J.R., Cooke, M.L., Sussman, A.J., 2005. Evidence for temporally changing mechanical stratigraphy and effects on joint-network architecture. Geology 33 (2), 101–104.
Sperrevik, S., Gillespie, P.A., Fisher, Q.J., Halverson, T., Knipe, R.J., 2002. Empirical estimation of fault rock properties. In: Koestler, A.G., Hunsdale, R. (Eds.), Hydrocarbon Seal Quantification, NPF Special Publication, Vol. 11. Elsevier, Amsterdam, pp. 109–125.
Sterling, S.N., Parker, B.L., Cherry, J.A., Williams, J.H., Lane, J.W., Haeni, F.P., 2005. Vertical cross contamination of trichloroethylene in a borehole in fractured sandstone. Groundwater 43 (4), 557–573.
Terzaghi, R.D., 1965. Sources of error in joint surveys. Geotechnique 15 (3), 287–304.
Tondi, E., Cilona, A., Agosta, F., Aydin, A., Rustichelli, A., Renda, P., Giunta, G., 2012. Growth processes, dimensional parameters and scaling relationships of two conjugate sets of compactive shear bands in porous carbonate grainstones, Favignana Island, Italy. J. Struct. Geol. 37, 53–64.
Torabi, A., Berg, S.S., 2011. Scaling of fault attributes: a review. Mar. Petrol. Geol. 28 (8), 1444–1460.
Twenter, F.R., Metzger, D.G., 1963. Geology and Ground Water in Verde Valley—the Mogollon Rim Region, Arizona, vol. 1177. US Government Printing Office.
Twiss, R., Marrett, R., 2010. Determining brittle extension and shear strain using fault length and displacement systematics: part I: theory. J. Struct. Geol. 32, (12), 1960–1977.
Wardlaw, N.C., Taylor, R.P., 1976. Mercury capillary pressure curves and the interpretation of pore structure and capillary behavior in reservoir rocks. Bull. Can. Petrol. Geol. 24 (2), 225–262.
Weber, K.J., 1982. Influence of common sedimentary structures on fluid flow in reservoir models. J. Petrol. Technol. 34 (3), 665–672.
Wu, H., Pollard, D.D., 1995. An experimental study of the relationship between joint spacing and layer thickness. J. Struct. Geol. 17 (6), 887–905.
Yeats, R.S., 1987. Changing tectonic styles in Cenozoic basins of Southern California. In: in Ingersoll, R.V., Ernst, W.G. (Eds.), Cenozoic Basin Development of Coastal California. Prentice Hall, Englewood Cliffs, New Jersey, pp. 284–298. Rubey Volume VI.
Yeats, R.S., Huftile, G.J., Stitt, L.T., 1994. Late Cenozoic tectonics of the east Ventura Basin, transverse ranges, California. AAPG Bull. 78 (7), 1040–1074.
Yerkes, R.F., Campbell, R.H., 2005. Preliminary Geologic Map of the Los Angeles 30′ x 60′ Quadrangle, Southern California. USGS Open-File Report 2005–1019.
Yielding, G., Freeman, B., Needham, D.T., 1997. Quantitative fault seal prediction. AAPG Bull. 81 (6), 897–917.